

AD-A066 595

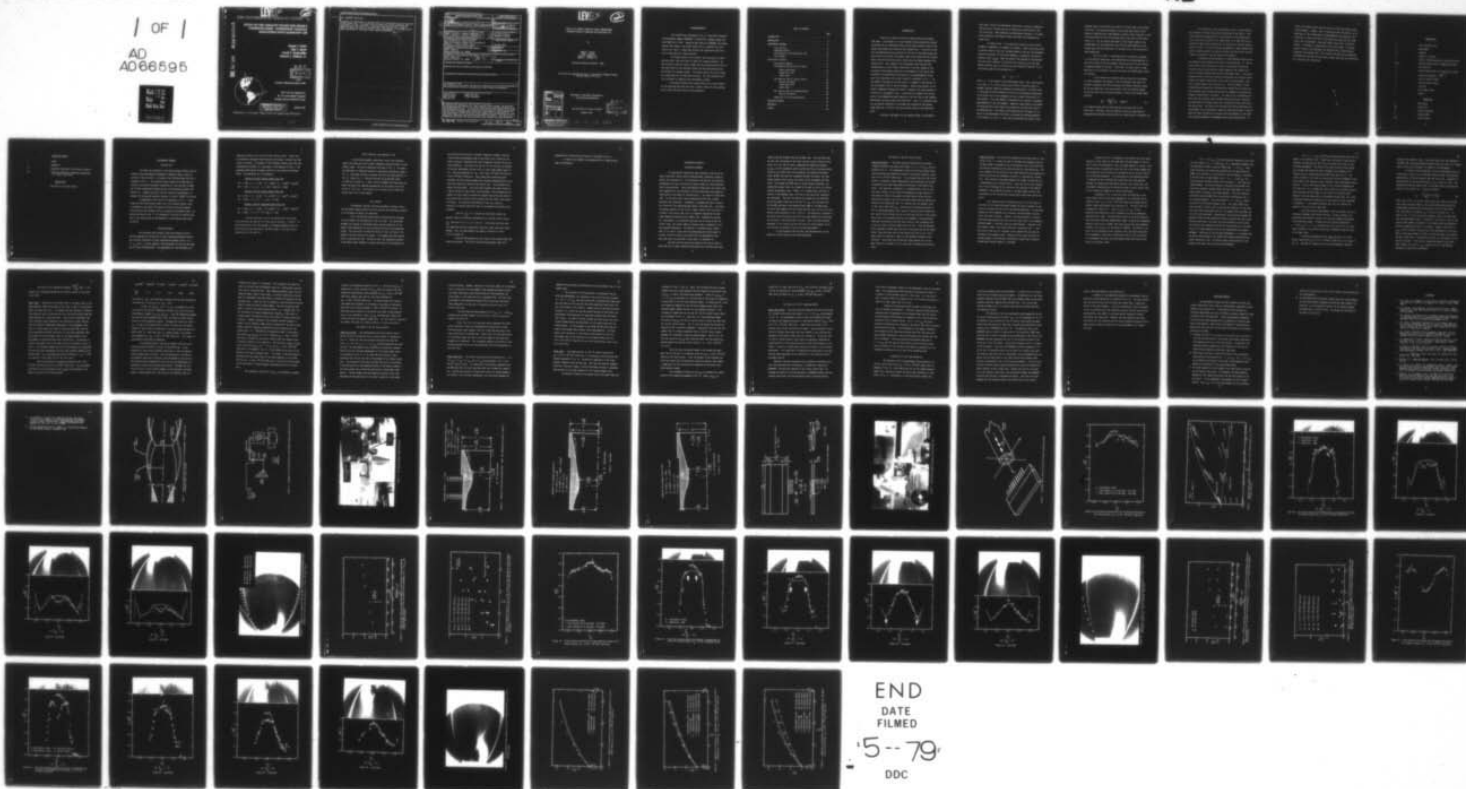
TEXAS UNIV AT AUSTIN DEPT OF AEROSPACE ENGINEERING AN--ETC F/G 21/2
STUDY OF THE EXHAUST PLUME FOR HIGHLY UNDEREXPANDED SUPERSONIC --ETC(U)
JAN 79 S J SUTTER, J J BERTIN, E J ZIHLMAN DAAK40-77-C-0131

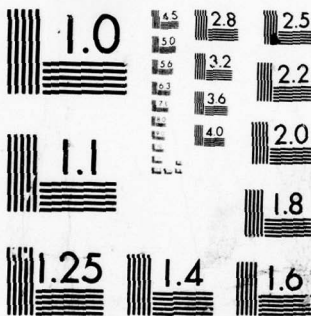
UNCLASSIFIED

79001

NL

| OF |
AD
A066595





MICROCOPY RESOLUTION TEST CHART
NATIONAL BUREAU OF STANDARDS-1963-A

LEVEL II

2

THE UNIVERSITY OF TEXAS AT AUSTIN

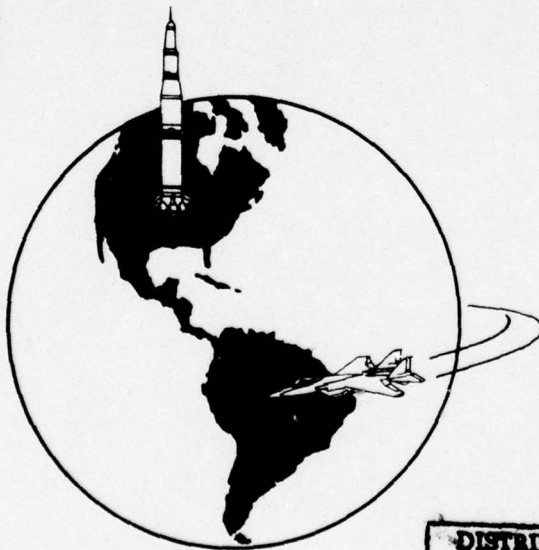
AD A0 66 595

STUDY OF THE EXHAUST PLUME FOR HIGHLY UNDEREXPANDED SUPERSONIC NOZZLES EXHAUSTING INTO QUIESCENT AIR

**Samuel J. Sutter
John J. Bertin
David P. Dannemiller
Edward J. Zihlman, Jr.**

DDC FILE COPY

**DDC
RECEIVED
MAR 30 1979
MCD**



Aerospace Engineering Report 79001

**This work was supported by
the U.S. Army Missile Command
through contract DAAK40-77-C-0131**

**DISTRIBUTION STATEMENT A
Approved for public release;
Distribution Unlimited**

January 1979

Department of Aerospace Engineering and Engineering Mechanics

79 03 26 167

20. ABSTRACT Continued...

regarding the fabrication of hardware which will successfully control the flow in the annular gap. The report also discusses the current attributes and shortcomings of the University's numerical codes and provides a range of empirical data with which to evaluate future developments in the codes and to make assessments of continued rocket system advancements.

[Faint, mostly illegible text, possibly bleed-through from the reverse side of the page]

[Faint, mostly illegible text, possibly bleed-through from the reverse side of the page]

[Faint, mostly illegible text, possibly bleed-through from the reverse side of the page]

[Faint, mostly illegible text, possibly bleed-through from the reverse side of the page]

REPORT DOCUMENTATION PAGE		READ INSTRUCTIONS BEFORE COMPLETING FORM
1. REPORT NUMBER AER 79001	2. GOVT ACCESSION NO.	3. RECIPIENT'S CATALOG NUMBER
4. TITLE (and Subtitle) Study of the Exhaust Plume for Highly Underexpanded Supersonic Nozzles Exhausting Into Quiescent Air,		5. REPORT DATE AND PERIOD COVERED Final rept. Jul 77- Aug Sep 78,
6. AUTHOR(s) Samuel J. Sutter, Edward J. Zihlman, Jr. John J. Bertin, David P. Dannemiller		7. PERFORMING ORG. REPORT NUMBER
9. PERFORMING ORGANIZATION NAME AND ADDRESS The University of Texas at Austin Dept of Aerospace Engineering & Engineering Mechanics - Austin, Texas 78712		8. CONTRACT OR GRANT NUMBER(s) DAAK40-77-C-0131
11. CONTROLLING OFFICE NAME AND ADDRESS Commander, US Army Missile R&D Command ATTN: DRDMI-TI Redstone Arsenal, AL 35809		10. PROGRAM ELEMENT, PROJECT, TASK AREA & WORK UNIT NUMBERS DD Form 1498
14. MONITORING AGENCY NAME & ADDRESS (if different from Controlling Office) Commander, US Army Missile R&D Command ATTN: DRDMI-TLH Redstone Arsenal, AL 35809		12. REPORT DATE Jan 79
		13. NUMBER OF PAGES 73
		15. SECURITY CLASS. (of this report) UC
		15a. DECLASSIFICATION/DOWNGRADING SCHEDULE
16. DISTRIBUTION STATEMENT (of this Report) Approved for Public Release; Distribution Unlimited		
17. DISTRIBUTION STATEMENT (of the abstract entered in Block 20, if different from Report)		
18. SUPPLEMENTARY NOTES The findings of this report are not to be construed as an official Department of the Army position unless so designated by other authorized documents.		
19. KEY WORDS (Continue on reverse side if necessary and identify by block number) Exhaust Plume Numerical Code Tube Launcher Plume Impingment Blow-by Flow		
20. ABSTRACT (Continue on reverse side if necessary and identify by block number) To optimize the performance of a tube launched rocket system, the mechanism which generates the flow in the annular gap must be accurately modeled during the system design phase. The present program defines the exhaust plume which results when an underexpanded, supersonic steam exhausts into quiescent air. The free plumes of three different nozzle geometrical configurations are com- pared with theoretical method-of-characteristic solutions. The results are a foundation upon which the tube-launched rocket designer may base decisions		

LEVEL II

2

STUDY OF THE EXHAUST PLUME FOR HIGHLY UNDEREXPANDED SUPERSONIC NOZZLES EXHAUSTING INTO QUIESCENT AIR*

by

Samuel J. Sutter
John J. Bertin
David P. Dannemiller
Edward J. Zihlman, Jr.

Aerospace Engineering Report 79001

*This work was supported by the U.S. Army Missile Command through
Contract DAAK 40-77-C-0131

AUTHORITY BY	
DTIC	Wallo Center <input checked="" type="checkbox"/>
DDC	Def Center <input type="checkbox"/>
UNASSIGNED	<input type="checkbox"/>
JUSTIFICATION	
DTIC DISTRIBUTION/AVAILABILITY CODES	
DTIC	AVAIL. and/or SPECIAL
A	

Department of Aerospace Engineering
and Engineering Mechanics

The University of Texas at Austin

January 1979

DDC
RECEIVED
MAR 30 1979
REGISTERED
D

DISTRIBUTION STATEMENT A

Approved for public release;
Distribution Unlimited

79 03 26 167

ACKNOWLEDGEMENTS

This research was supported by the U.S. Army Missile Research and Development Command (MIRADCOM) in Huntsville, Alabama through Contract DAAK-40-77-C-0131. Among the many people at MIRADCOM who helped provide this support, the authors would like to recognize the assistance of Mr. David L. Booker who provided the organization and direction to help make this report possible.

The authors would like to express their gratitude to others who gave their time and efforts to make this research possible. Mr. Henry Franklin deserves special thanks for the excellent work he did in the fabrication of the simulated rockets and the experienced advice he provided for hardware design. The authors would also like to thank Mr. Johnny Reed for his fabrication efforts. Mr. Mark Melanson skillfully assisted in conducting the experimental program.

The authors express their appreciation to Ms. Janet Simpson for the drafting work done and to Mrs. Bettye Lofton for her excellent job of typing the many drafts of the manuscript.

TABLE OF CONTENTS

	Page
INTRODUCTION	1
NOMENCLATURE	6
EXPERIMENTAL PROGRAM	8
Test Facility	8
Simulated Rockets	8
Pitot Probes for the Supersonic Flow	10
Test Program	10
DISCUSSION OF RESULTS	13
Introductory Remarks	13
The Plume for the 20° Conical Nozzle	15
Nozzle exit-plane	15
Plume flow field	16
Shear layer	21
The Plume for the 10° Conical Nozzle	24
Nozzle exit-plane	24
Plume flow field	25
Shear layer	26
The Plume for the 10° Contoured Nozzle	28
Nozzle exit-plane	28
Comparison of the Plume Boundaries	29
CONCLUDING REMARKS	32
REFERENCES	34
FIGURES	36

INTRODUCTION

There are a variety of military rockets which are launched from tubes. The designer of a tube-launched rocket system must consider the possibility of unbalanced forces on the rocket caused by flow in the annular gap between the rocket and the launcher wall. To be able to predict the magnitude and the direction of the flow in the annular gap, one must be able to describe the exhaust plume of the rocket and the viscous/shock interaction structure which results when the plume encounters the launcher wall. The strength of the impingement shock wave and the characteristics of the viscous interaction at the wall depend on the structure of the exhaust plume and on the geometry of the launch tube. A sketch of the generalized flow pattern of an underexpanded, axisymmetric jet exhausting into a static medium is presented in Fig. 1. As the exhaust flow emerges from the nozzle, it expands to the pressure of the surrounding fluid at the jet boundary. Because the pressure of the ambient atmosphere bounding the plume is constant, the plume boundary is curved for an axisymmetric flow. A shock wave is formed by the coalescence of the compression waves required to turn the flow at the boundary. Downstream, the shock waves form a Mach disc. Thus, it is important that one can develop techniques to calculate the structure of the exhaust plume (both the "inviscid" core and the shear layer at the plume boundary).

To develop flow models for the exhaust plumes, investigators

have used a variety of experimental simulations, varying in complexity from the use of cold-gas jets to an almost exact duplication of the full-scale jets. When conducting an experimental program, it is important to establish the degree to which the model flow simulates the actual flow.

As noted in Ref. 1, the shape and curvature of the inviscid boundary is dependent on a number of variables. These include the ratio of specific heats of the jet, the Mach number of the jet, the divergence angle of the nozzle (or the nozzle geometry, in general), and the jet pressure ratio, p_{ne}/p_b . When the exhaust flow expands (or accelerates) from the static pressure in the nozzle exit plane (p_{ne}) to the lower ambient pressure (p_b), an inviscid jet would expand so that the initial inclination angle of the expanded jet is:

$$\theta_{p,0} = \theta_{ne} + \Delta v \quad (1)$$

where Δv is the change in the Prandtl-Meyer angle. Most investigators, e.g., Refs. 1, 2, 3, and 4 believe the initial inclination angle is, perhaps, the most important property to be duplicated. As noted in Ref. 2, the shape of the jet boundary for the first few diameters downstream of the nozzle exit can be assumed to be only slightly affected by viscous effects. Thus, the method of characteristics provides a reasonable approximation for the jet boundary. Numerical codes based on the method of characteristics can be used to calculate the inviscid flow field of the expanding jet. Such codes, while neglecting the influence of viscosity on the downstream flow field, can account for entropy gradients in the plume, e.g., Ref. 5. Thus, one can represent the effect of the

boundary layer at the nozzle exit plane or of shock waves in the plume flow field. The accuracy obtained in the actual application of the method-of-characteristics code depends on factors such as how well is the flow field known for the initial plane used at the start of the calculation (i.e., for the nozzle exit-plane in the present report), the assumed model for the downstream flow, the non-ideal behavior of the exhaust gas, and the construction of the mesh size as the solution proceeds downstream.

Love et al (Ref. 1) concluded that "a circular-arc boundary is a satisfactory prediction, both theoretically and experimentally, of the first portion of the jet boundary from the jet exit to the vicinity of maximum diameter of the jet". Korst (Ref. 4) states that if plume modeling is to be achieved, one must also match the dimensionless radius of curvature.

If the condition of constant pressure along the jet boundary is used to determine the changes in the jet boundary angle which are required to compress the flow and balance the pressure decrease caused by the one-dimensional flow area increase, then the relation between the turning angle and the pressure change is given by the Prandtl-Meyer relation:

$$\frac{\Delta p}{p} = \frac{\gamma(M_{ne})^2}{\beta_{ne}} (\Delta v) + \mathcal{O}(\Delta v)^2 \quad (2)$$

It is apparent then, that two jets that have the same value of the coefficient $\gamma(M_{ne})^2/\beta_{ne}$ could be expected to have the same pressure-change/deflection-angle relation within the linearization of equation (2).

The simulation of the nozzle exhaust flow is complicated by the presence of oblique shock waves originating in the nozzle. Such shock waves may be generated by a discontinuity of the second derivative of the nozzle contour at the throat (Ref. 6) or when the flow is turned back toward the centerline by an inflection in the wall contour. Leng et al (Ref. 7) caution that the impingement of these oblique shock waves on nearby surfaces can radically affect the flow field, the heat-transfer distribution, and the pressure distribution.

To optimize the performance of a tube-launched rocket system, the mechanism which generates the flow in the annular gap, i.e. the exhaust plume of the rocket nozzle and the viscous/shock interaction structure which results when the plume encounters the launcher wall, must be accurately modeled during the system design phase. The present program defines, with pitot-pressure distributions and schlieren photographs, the exhaust plume which results when an underexpanded, supersonic stream exhausts into quiescent air. The free plumes of three different nozzle geometrical configurations appropriate to present day tube-launched rocket system applications are compared with theoretical method-of-characteristic solutions. The results are a foundation upon which the tube-launched rocket designer may base decisions regarding the fabrication of hardware which will successfully control the flow in the annular gap. The report also discusses the current attributes and shortcomings of the University's numerical codes and provides a range of empirical data with which to evaluate future developments in the codes and to make assessments of continued rocket system advancements. By

itself, the present report does not totally satisfy the present needs of the designer. However, used in conjunction with the results, to be published, of the second phase of experimentation now ongoing at the University of Texas, the flow in the annular gap should be well understood, and, consequently, steps made toward controlling its adverse effects. Following is a description of the free plumes. The second report, "Study of the Impinging Flow Produced when a Rocket Exhaust Encounters the Launcher Wall", will examine the same nozzle geometrical configurations and describe the exhaust plumes when they are constrained by a constant area launch tube.

NOMENCLATURE

A	cross sectional area
M	Mach number
p	pressure
R	radius of curvature
r	radius, distance measured in radial direction
Re_{θ}	Reynolds number based on momentum thickness
U	flow velocity
\tilde{x}	distance downstream of the nozzle-exit plane
β	simulation parameter, $\sqrt{M^2 - 1}$
γ	ratio of specific heats
θ	flow inclination angle
μ	viscosity
ν	Prantl-Meyer angle
ρ	density

Subscripts

b	base region
ne	nozzle exit
0	initial condition
p	exhaust plume
pit	pitot pressure

Subscripts (Cont.)

r	rocket
t	stagnation
t1	stagnation conditions in the nozzle reservoir
t2	stagnation conditions immediately downstream of a normal shock wave

Superscripts

*	evaluated at the nozzle throat
---	--------------------------------

EXPERIMENTAL PROGRAM

Test Facility

The tests were conducted at the Rocket Exhaust Effects Facility located at the Experimental Aerodynamics Laboratory (EAL) of the University of Texas at Austin. A diagram of the blow-down type facility is presented in Fig. 2. The simulated rocket exhaust jet plumes were obtained by accelerating unheated, compressed air (the test gas) through one of three convergent-divergent nozzles (the simulated rockets) into ambient air. Steady state test time was limited to approximately 14 seconds for the maximum reservoir pressure of $9.046 \times 10^6 \text{ N/m}^2$ (1312 psia).

A photograph of the facility is presented in Fig. 3. Illustrated are the high pressure supply line, the simulated rocket, which is threaded to the supply line and held firmly by the yoke assembly, and the pitot-probe assembly, which is mounted on the movable table. By moving the table in the \tilde{x} (or streamwise) direction the relative location of the pitot-pressure instrumentation in the exhaust plume could be varied.

Simulated Rockets

The simulated rocket exhaust flows were produced by accelerating unheated air through one of three convergent/divergent nozzles. The principal dimensions of these convergent/divergent nozzles, i.e., r^* , r_{ne} , and r_r , and the contour of the convergent section were the same for all three configurations. The coordinates for the convergent sec-

section are given in Fig. 4a for the 20° conical nozzle. (Since the \tilde{x} coordinate is measured from the nozzle exit-plane, it would vary from nozzle to nozzle). The contour of the divergent section, which was the configuration variable, is illustrated in the sketches of Fig. 4. The equations defining the divergent section for each nozzle are defined below. The dimensions are in centimeters.

Nozzle A, the 20° conical nozzle (Fig. 4a):

$$\text{For } -1.308 \leq \tilde{x} \leq -1.031: (\tilde{x} + 1.308)^2 + (r - 1.626)^2 = (0.813)^2$$

$$\text{For } -1.031 \leq \tilde{x} \leq 0.0: r = 0.759 + 0.364 (\tilde{x} + 1.308)$$

Nozzle B, the 10° conical nozzle (Fig. 4b):

$$\text{For } -2.479 \leq \tilde{x} \leq -2.338: (\tilde{x} + 2.479)^2 + (r - 1.626)^2 = (0.813)^2$$

$$\text{For } -2.338 \leq \tilde{x} \leq 0.0: r - 1.237 = 0.176\tilde{x}$$

Nozzle C, the 10° contoured nozzle (Fig. 4c):

$$\text{For } -2.098 \leq \tilde{x} \leq -1.895: (\tilde{x} + 2.098)^2 + (r - 1.626)^2 = (0.813)^2$$

$$\text{For } -1.895 \leq \tilde{x} \leq 0.0: r^2 = 0.434 \tilde{x} + 1.530$$

The cross-sectional area of the throat and of the nozzle exit-plane were the same for all three nozzles with $A_{ne} = 2.316 A^*$. If the acceleration of the flow through a convergent/divergent nozzle of this area ratio were isentropic, the Mach number in the nozzle exit-plane would be 2.36 (Ref. 8).

Pitot Probes for the Supersonic Flow

A pitot-probe assembly containing a row of nine stainless steel pitot tubes was used to sense stagnation pressure profiles in the exhaust plume. The rake's dimensions are shown in Fig. 5. The tubes were mounted in a wedge and secured to the movable platform as shown in Fig. 6. The probes could be traversed laterally and longitudinally in the $\tilde{x}r$ plane, Fig. 7. Position accuracy was maintained within ± 0.0076 cm (± 0.003 in.). After initial alignment the probes were not moved vertically and remained perpendicular to the nozzle exit-plane during all test runs. The pressures were recorded using 0-1000 psig Bourdon-type dial pressure gauges.

Test Program

The apparatus and data-recording equipment currently used at the EAL Rocket Exhaust Effects Facility required the following procedure to be followed to conduct the experiment.

First, the desired rocket nozzle configuration was threaded into the supply line and anchored to the rail yoke. The pitot-probe assembly was secured to the movable table and the centerline of the middle probe aligned so as to be collinear with that of the simulated rocket. The traversible carriage was moved to place the plane of the probes in the exit plane of the nozzle. The assembly was then secured prior to starting the flow. During the test, the stagnation pressure in the nozzle (and, therefore, the mass flow rate of the unheated air)

was controlled to maintain a constant stagnation (chamber) pressure. Pitot-pressure measurements made in the supply line, serving as the nozzle reservoir, determined the local stagnation pressure during system calibration. The velocity of the air in this line was not negligible but was determined, by area ratio, to have a Mach number equal to 0.4. Data were obtained for p_{t1} from $1.462 \times 10^6 \text{ N/m}^2$ (212 psia) to $8.715 \times 10^6 \text{ N/m}^2$ (1264 psia). Once steady-state conditions were achieved, the dial pressure gauges were recorded photographically and a schlieren picture was taken of the exhaust flow. This procedure produced nine data points. The pitot-probe assembly was moved laterally 0.064 cm (0.025 in) and another test performed. This procedure was repeated five more times to provide 54 original data points and nine repeat points which could be used to define the flow field in the nozzle exit-plane. The detailed investigation of the exit plane was necessary to provide sufficient input to the method-of-characteristics programs.

Once the $\frac{\tilde{x}}{r_{ne}} = 0.0$ station was thoroughly probed, the movable table was traversed longitudinally to provide similar data at $\frac{\tilde{x}}{r_{ne}}$ stations of 0.5, 1.0, 2.0, and 3.0. Since these data were used for comparison with the theoretical solutions, fewer data points were needed. Thus, the measurements were made at intervals of every 0.127 cm (0.050 in).

Schlieren photographs were also taken of the plume without the pitot rake present. The facility permitted photographs taken only

perpendicular to the nozzle exit-plane as indicated in Fig. 3.

A similar run schedule was completed for all three nozzles under investigation.

DISCUSSION OF RESULTS

Introductory Remarks

An experimental program has been conducted to define the exhaust plume which results when an underexpanded, supersonic stream exhausts into quiescent air. Pitot-pressure distributions and schlieren photographs were used to define the exhaust plumes for three different nozzle configurations. These experimentally-determined flow fields have been compared with the theoretical solutions generated using numerical codes based on the method of characteristics. Two numerical codes were used. For the more simple code, designated the MOC code, entropy gradients were neglected. Furthermore, no attempt was made to control the location of the downstream mesh points in the MOC code. The effect of entropy gradients in the initial (input) plane of the flow field is included in the second code, which is therefore designated the Rotational Method-of-Characteristics (RMOC) code. Although the entropy (or, equivalently, the stagnation pressure) can be varied across the initial plane, the entropy remains constant along a streamline as the flow proceeds downstream. The Hartree, or reference plane, method (Ref. 9) is used to insure that the downstream mesh points remain in a plane, thus facilitating correlation with the experimental data. These two codes are described in more detail in Reference 10.

Starting from the nozzle exit-plane as the initial plane in which the flow is known, method-of-characteristics solutions were gene-

rated using both the MOC code and the RMOC code. The local Mach number (M), the inclination of the local velocity vector relative to the nozzle axis (θ), and the local, dimensionless stagnation pressure (p_t/p_{t1}) are the parameters used to define the flow at the mesh points. Values for any other flow field parameters were derived from these. Since the MOC code does not accommodate entropy variations, the stagnation pressure ratio (p_t/p_{t1}) was equal to one throughout the flow field. Even though the RMOC code can handle entropy gradients, the stagnation pressure ratio was assumed to be equal to one at all points outside the boundary layer. Hence, it is assumed that, with the exception of the boundary layer, the flow in the nozzle was isentropic for both codes. The flow inclination was assumed to vary uniformly across the nozzle from zero at the axis to θ_{ne} (at the nozzle wall for the MOC code and at the boundary-layer edge for the RMOC code). The local Mach numbers were calculated from the curve fits of the pitot-pressure data presented in Figs. 8 and 14. The theoretical solutions of the plume flow fields were essentially the same whether the third-order fit was used or the fourth-order fit used. Thus, the plume solutions presented in this section use the particular fit which appears to provide the best correlation of the exit-plane measurements.

In the discussion that follows, the characteristics of the plume for a given nozzle are discussed separately.

The Plume for the 20° Conical Nozzle

Nozzle exit-plane. - The pitot pressures measured with the probe assembly located at the nozzle exit-plane, i.e., $\tilde{x} = 0.0 r_{ne}$, are presented in Fig. 8. The experimental values of the pitot pressure have been divided by the stagnation pressure in the nozzle reservoir, which was $8.715 \times 10^6 \text{ N/m}^2$ (1264 psia). If one assumes that the flow in the nozzle is isentropic, these dimensionless pitot pressures can be used to determine the radial Mach number distribution in the nozzle exit-plane. The isentropic assumption is a reasonable one, since (1) the only waves evident in the schlieren photographs are near the wall of the nozzle and they do not appear to significantly affect the exit plane pitot pressures, and (2) calculations made using the University's version of the BLIMP code (Ref. 11) indicate that the boundary layer is thin (less than $0.025 r_{ne}$). Referring to the tabulated values of Ref. 8, these experimental pitot pressures indicate that the Mach number varies from 2.23 near the axis to 2.48 near the wall of the nozzle. Recall that if one assumes that the flow undergoes a one-dimensional, isentropic acceleration from the sonic throat to the streamtube area of the exit plane, the Mach number would be 2.36. Since the measured pitot pressures indicate that the flow in the nozzle was not one dimensional, these data were used to help define the flow in the initial plane, which is required as input for the method-of-characteristics solutions. Third-order and fourth-order least-squares fits of the data, which are included in Fig. 8, were used to generate the correlations.

Plume flow field. - The flow field computed using the MOC code is illustrated in Fig. 9. Arrows are used to represent the computed values of the Mach number (indicated by the arrow lengths) and of the local flow inclination (indicated by the arrow direction) at selected points. The inner boundary of that portion of the plume affected by the expansion of the exit-plane flow to atmospheric pressure is indicated by a broken line. That portion of the plume between this broken line and the axis is designated as the "internal core". Since the flow in this internal core is not influenced by the relatively low pressure of the ambient atmosphere, the streamwise increase in the Mach number reflects the continuation of the acceleration process which takes place within the nozzle.

The "expansion fan" indicated near the lip of the nozzle is the result of the large difference between the static pressure in the nozzle exit-plane and that of the surrounding atmosphere. As the plume expands and the streamtube area increases, the Mach number at points within the plume increases. However, since the pressure is constant along the plume boundary and since the free shear-layer is not modeled, the Mach number is constant along the plume boundary. Therefore, the Mach number varies in the radial direction, increasing with r from the value at the axis to a maximum in the expansion fan and then decreasing to the boundary value. Because of this radial variation in the Mach number, pitot-pressure distributions should have a relative minimum when the Mach number is a maximum.

Because the flow is axisymmetric and because the local static pressure in that region of the plume where the Mach number is the largest is below the atmospheric value, the plume boundary is curved. Compression waves are generated to turn the flow at the plume boundary and to increase the static pressure at the edge of the jet to the value of the surrounding atmosphere. The coalescence of the compression waves is indicated by the "intersecting" arrows near the plume boundary. Although the compression waves would coalesce into a shock wave, the flow models represented by the University codes in their present form do not include the formation of internal shock waves.

Presented in Fig. 10 are the radial distributions of the pitot pressure which result when unheated air is accelerated from a reservoir where p_{t1} is $8.715 \times 10^6 \text{ N/m}^2$ (1264 psia) through the 20° conical nozzle and exhausts into quiescent air. The data, which are presented for values of \tilde{x} from $0.5 r_{ne}$ to $3.0 r_{ne}$, are compared with the theoretical values computed using the two method-of-characteristics codes. The theoretical values of the pitot pressures were calculated using the computed Mach number to define the stagnation pressure ratio across a normal shock wave (p_{t2}/p_t) and the stagnation pressure ratio (p_t/p_{t1}) for the point of interest. The effect of the local flow inclination was not included in the calculation procedure. This "assumption" could have a significant effect on the correlation in the expanded flow near the plume boundary where the flow inclinations are relatively large.

For $\tilde{x} = 0.5 r_{ne}$, the pitot pressures measured in the internal core region (i.e., $r < 0.965 r_{ne}$) are in reasonable agreement with the theoretical values, except for those near $r = 0.5 r_{ne}$. Since these relatively low values were obtained with the same probe and appear to be peculiar to these few runs, the discrepancy is believed to be the result of experimental error. For $r > 0.965 r_{ne}$, the pitot pressures decrease rapidly with increasing r until near the plume boundary. The pitot pressures calculated using the MOC flow field pass through a minimum (where the local Mach number is a maximum) and then increase to the plume boundary. The pitot pressures calculated using the RMOC flow field decrease continuously with r to the plume boundary. The calculations for $r > 1.20 r_{ne}$ exhibit the effects of the nozzle boundary layer. The reader should note that the model currently used to describe the expansions of the boundary layer needs improvement and will be changed (since the RMOC code is still being developed). Nevertheless, the correlation between the measured values and the theoretical values indicates that the viscous effects significantly influence the pitot pressures in this region. The detailed data required to define the pitot pressures in the shear layer at the plume boundary could not be obtained with the present equipment. Referring to the schlieren photographs, it is evident that the actual plume boundary lies outside the location predicted using either theoretical code. At present neither code accounts for the growth of the shear layer along the plume boundary.

For $\tilde{x} \geq 1.0 r_{ne}$, the pitot pressures measured near the axis appear to be relatively low. A weak wave, indicating a large density gradient, originating near the lip of the nozzle can be seen in the schlieren photograph. The trace of this wave follows closely (being just inside) the broken line which represents the boundary of the internal core as calculated using the MOC code (see Fig. 9). The radial location of this wave at a particular station corresponds to the outer edge of the "pressure valley" observed in the experimental distributions. Since no shock waves appear in the schlieren photograph of the inner core, it is assumed that these relatively low pitot pressures result because the Mach number in this region is relatively high. Numerical solutions generated at the Redstone Arsenal (Ref. 12), using a rotational method-of-characteristics code similar to that described in Reference 5, correspond reasonably well with the results presented for the University's RMOC code.

The pitot-pressure measurements from the expansion fan are in reasonable agreement with the MOC solution. At most stations, the experimental distribution exhibits the relative minimum corresponding to the peak Mach number. Although the pitot pressure measured at $r = 1.82 r_{ne}$ at $\tilde{x} = 1.0 r_{ne}$ indicates that this point was in the shear layer, the data do not provide significant information about the flow in the shear layer.

A schlieren photograph of the plume generated for the 20° conical nozzle with p_{t1} of $8.715 \times 10^6 \text{ N/m}^2$ (1264 psia) is presented in Fig. 11. Included for comparison are the plume boundaries computed

using the two numerical codes. Note that despite the shortcomings of the RMOC code, the plume boundary computed using this code lies slightly nearer to the actual boundary, as evident in the photograph.

As noted in the Introduction, various investigators have concluded that a circular arc of constant radius provides a satisfactory approximation of the jet boundary near the nozzle exit. Equation (1) has been used to calculate the value of $\theta_{p,0}$ which is 41.33° . The method prescribed by Pindzola (Ref. 2) has been used to calculate the radius of the circular arc. Using the relation:

$$R_p = \frac{15.7 r_{ne}}{M_{ne}} \sqrt{5 + M_{ne}^2} \quad (3)$$

where $M_{ne} = 2.475$ for the 20° conical nozzle was taken from the MOC code as the last Mach number in the radial distribution before the Prandtl-Meyer expansion was constructed at the lip of the nozzle. Thus, the radius of curvature, R_p , is 26.173 cm (10.304 in.). As shown in Fig. 11, the "circular-arc boundary" did not correlate well with the experimental plume. Variations in the value of M_{ne} for the range of Mach numbers considered in the present study had negligible effect on changing the radius of curvature. However, the value of $\theta_{p,0}$ and the resultant construction of the perpendicular to the tangent of the plume boundary in order to locate the center of curvature was most significant in locating the circular arc with respect to the nozzle exit-plane. Since the arc exceeds the bounds of the experimental plume, the value of $\theta_{p,0}$ would have to be significantly decreased to improve the correlation.

The value of the simulation parameter $\frac{\gamma(M_{ne})^2}{\beta_{ne}}$ (Ref. ?) for the gas (air) exhausted through the 20° conical nozzle is calculated to be 3.788.

Shear layer. - Definition of the growth rate of the shear layer at the plume boundary should be included in the code, if one is to accurately model the plume flow field. It becomes even more important in developing analytical tools to describe the flow field which results when the plume impinges on a launch-tube wall. Data (as yet unreported) from tests currently being conducted at the University of Texas indicate that the pressures immediately downstream of the impingement shock wave in a launch tube are as much as twenty percent lower than the value predicted by the MOC code which, as previously mentioned, does not account for the free-shear layer at the plume boundary or the development of shock-wave/shear-layer interactions. Correlations related to the growth rate of the shear layer are presented in Figs. 12 and 13. The distance between the actual plume boundary (as determined from the schlieren photographs) and the plume boundary computed using the MOC code, Δr_p , (non-dimensionalized by dividing by r_{ne}) is used as a measure of the growth rate of the shear layer.

Data are presented for stagnation pressures from 1.462×10^6 N/m² (212 psia) to 8.715×10^6 N/m² (1264 psia). The corresponding values of the jet-pressure ratio (p_{ne}/p_b) are presented in the table at the top of the following page.

p_{t1} (N/m ²)	1.462×10^6	2.779×10^6	4.102×10^6	6.074×10^6	8.715×10^6
$\frac{p_{ne}}{p_b}$	1.111	2.111	3.116	4.614	6.621

The values of p_{ne} were calculated assuming that the flow accelerated isentropically in the nozzle to $M_{ne} = 2.36$.

In Fig. 12, $\Delta r_p / r_{ne}$ at $\tilde{x} = 1.0 r_{ne}$ is presented as a function both of the reservoir stagnation pressure (p_{t1}) and of the exit-plane Reynolds numbers ($\rho_{ne} U_{ne} r_{ne} / \mu_{ne}$). Since the stagnation temperature and the nozzle geometry were fixed, the Reynolds number depends directly on the stagnation pressure. Although the nozzle-exit radius r_{ne} is used as the characteristic length, the choice of the proper length for nozzle flows is uncertain, as has been stated previously by Herron (Ref. 3). Note that there is a marked change in the growth rate parameter for $p_{t1} > 4.102 \times 10^6$ N/m² (595 psia). This change is attributed to the onset of turbulence.

As discussed earlier, the nozzle boundary layer was calculated using the University's version of the BLIMP code. It was necessary to input certain boundary conditions in order to generate these boundary-layer solutions. The flow parameters at the edge of the boundary layer were calculated using the geometric area ratio of the nozzle and the assumption that the flow was one-dimensional and isentropic to define the pressure distribution. Although the velocity of the air in the stilling chamber is not negligible (the Mach number is approximately 0.4), the effect of the boundary layer up-

stream of the throat was neglected. This assumption was based (in part) on the fact that the boundary layer for a continuously accelerating flow is relatively thin. When computing boundary layers for the Reynolds number range of these tests, a suitable transition criterion must be incorporated into the analysis to define the character of the boundary layer. Since the flow is supersonic, the transition criterion should include the effect of Mach number. One such transition parameter is used for the Space Shuttle Orbiter, i.e., (Re_{θ}/M) (Ref. 12). For the nozzle flow under consideration, $(Re_{\theta}/M)_{ne} = 342$, which is slightly above the baseline value of 270 used as a Shuttle transition criterion. However, because of the favorable pressure gradient, a higher critical Reynolds number would be expected for the nozzle flow. Indeed, values of $(Re_{\theta}/M)_{tr}$ approaching 400 were observed for the Shuttle (Ref. 12). Although the unit Reynolds number in the nozzle exit-plane $(\rho_{ne} U_{ne}/\mu_{ne})$ is $2.733 \times 10^8/m$ for $p_{t1} = 2.654 \times 10^6 \text{ N/m}^2$ (385 psia), solutions in the nozzle indicate that the boundary layer is entirely laminar at this condition. The relatively sudden increase in the values of $\Delta r_p/r_{ne}$ at $\tilde{x} = 1.0 r_{ne}$ for $p_{t1} > 4.102 \times 10^6 \text{ N/m}^2$ (595 psia), illustrated in Fig. 12, is attributed to the onset of turbulence in the nozzle boundary-layer. The reader is cautioned against concluding that the shear layer at the plume boundary is also turbulent for $p_{t1} > 4.102 \times 10^6 \text{ N/m}^2$ (595 psia), since the very large expansion at the nozzle lip would promote relaminarization of the viscous flow.

The streamwise variation of $\Delta r_p/r_{ne}$ is presented for several

values of the stagnation pressure in Fig. 13. Note that $\Delta r_p/r_{ne}$ is essentially a linear function of \tilde{x}/r_{ne} , with the slope of the line through the experimental values obtained for $p_{t1} \geq 6.074 \times 10^6 \text{ N/m}^2$ (881 psia) greater than that for the values obtained for $p_{t1} \leq 4.102 \times 10^6 \text{ N/m}^2$ (595 psia). As noted already, the change in the growth-rate parameter is attributed to the onset of turbulence. Note that for the data obtained at $1.462 \times 10^6 \text{ N/m}^2$ (212 psia), for which the static pressure in the nozzle exit-plane is approximately equal to the atmospheric value, $\Delta r_p/r_{ne}$ increases more slowly with \tilde{x} than the other low Reynolds number data. For this reservoir pressure, the exhaust flow does not expand rapidly as it leaves the nozzle.

The Plume for the 10° Conical Nozzle

Nozzle exit-plane. - The nondimensionalized pitot-pressure distribution for the exit-plane of the 10° conical nozzle is presented in Fig. 14. Except for the pitot pressures measured very near the axis, i.e., for $-0.2 r_{ne} < r < 0.2 r_{ne}$, and those measured very near the wall, the experimental pitot pressures are relatively constant. Referring to the schlieren photographs of the exhaust plume, which are presented in Fig. 15, it is clear that the relatively high pressures near the axis are due to the presence of an internal shock wave. The existence of this weak, oblique shock wave is attributed to discontinuities of the second derivative of the nozzle contour at the throat which occur during the fabrication of these small scale nozzles. The Mach number and the stagnation pressure of the flow downstream of the shock wave is less than it would be if the shock

were not present. However, because the local Mach number of the shocked flow is relatively low, the change in the stagnation pressure across the normal shock wave, which results when the flow encounters the pitot probe, is less than that for an unshocked flow. For this flow, the change in the stagnation pressure ratio across the pitot-probe shock compensates for decrease in stagnation pressure across the oblique shock wave.

The pitot-pressure measurements for $0.2 r_{ne} < |r| < 0.95 r_{ne}$ indicate that the Mach number in this portion of the exit plane was between 2.32 and 2.39.

Curve fits of all the data were used to generate the information required as input into the method-of-characteristics codes. The fourth-order least-squares curve fit of the data was used as the input correlation for the MOC code. Recall that, for the applications of the present codes, the flow in the core region of the nozzle was assumed to be isentropic. This assumption neglects the effects of the entropy gradients and of the shock-perturbed flow field parameters on the flow field.

Plume flow-field. - The radial pitot-pressure distributions for \tilde{x} of $0.5 r_{ne}$, $1.0 r_{ne}$, $2.0 r_{ne}$, and $3.0 r_{ne}$ are presented in Fig. 15 for the 10° conical nozzle. The theoretical distributions computed using the MOC code with the input described above are included for comparison. Despite the presence of shock waves, which are strong enough to be visible in the schlieren photographs, the correlation between the

computed pitot-pressure distributions and the experimental ones is reasonably good.

The locations of the shock waves, as determined from the schlieren photographs, are indicated by the arrows with the subsymbol "S". By $\tilde{x} = 3.0 r_{ne}$, the shock waves have intersected the plume boundary and there are no traces of the throat-generated shock waves visible in the plume at this station. Between the axis and the shock-wave location, i.e., where the flow has passed through the shock wave, the experimental pitot-pressures are measurably greater than the theoretical values. At radial locations outside the shock waves, the correlations between theory and experiment are very good except near the plume boundary. At the extremes of the plume the MOC again does not predict the minimum pitot pressure found experimentally. As noted before, this inaccuracy is attributed to deficiencies in the flow field model used in the code and to the increased effect that the local flow direction angularities near the plume boundary have on the pitot-probe data.

Shear layer - The plume boundary for the 10° conical nozzle with $p_{t1} = 8.715 \times 10^6 \text{ N/m}^2$ (1264 psia) is illustrated by the schlieren photograph presented in Fig. 16. Included for comparison is the plume boundary computed using the MOC code. Note that the solution computed using this relatively simple, inviscid flow model provides a reasonably good estimate of the plume boundary for this nozzle exhaust flow.

Correlations related to the growth rate of the shear layer are

presented in Figs. 17 and 18. Again, the nondimensionalized distance between the actual plume boundary and that computed using the MOC code, $\Delta r_p/r_{ne}$, is used as the growth-rate parameter. Values of $\Delta r_p/r_{ne}$ at $\tilde{x} = 1.0 r_{ne}$ are presented as a function both of the reservoir stagnation pressure and of the exit-plane Reynolds number. As noted earlier, since the stagnation temperature and the nozzle geometry were fixed, the Reynolds number depends directly on the stagnation pressure. Also included for comparison are the data for the 20° conical nozzle, which were presented in Fig. 12. Note that, at a given Reynolds number, the value of $\Delta r_p/r_{ne}$ for the 10° conical nozzle is much less than that for the 20° conical nozzle. This is true even though the nozzles are exhausting into a quiescent atmosphere. Apparently, the fact that the exhaust flow is already "spreading" more in the 20° conical nozzle promotes the "spreading" along the plume boundary. Recall (Fig. 13) that the values of $\Delta r_p/r_{ne}$ were relatively small for the properly expanded exhaust from the 20° conical nozzle, i.e., $1.462 \times 10^6 \text{ N/m}^2$ (212 psia).

Note also that the marked change in the growth-rate parameter due to the onset of turbulence occurs for $p_{t1} > 4.102 \times 10^6 \text{ N/m}^2$ (595 psia) for both nozzles. Since the lengths of the divergent sections are significantly different for these two nozzles, that length is apparently not the characteristic dimension for the nozzle exit-plane Reynolds number.

The streamwise variation of $\Delta r_p/r_{ne}$ is presented for several values of the stagnation pressure in Fig. 18. Again, $\Delta r_p/r_{ne}$ is

essentially a linear function of \tilde{x}/r_{ne} and distinctly different correlations are obtained for the measurements for $p_{t1} \geq 6.074 \times 10^6 \text{ N/m}^2$ (881 psia) and those for $p_{t1} \leq 4.102 \times 10^6 \text{ N/m}^2$ (595 psia).

The Plume for the 10° Contoured Nozzle

Nozzle exit-plane. - The pitot pressures measured with the probe assembly located at the nozzle exit-plane, i.e., $\tilde{x} = 0.0 r_{ne}$, are presented in Fig. 19. The experimental values of the pitot pressure have been divided by the stagnation pressure in the nozzle reservoir (p_{t1}), which was $8.715 \times 10^6 \text{ N/m}^2$ (1264 psia). Significant variations in the pressure occur across the nozzle exit-plane. These variations are the result of oblique shock waves which are evident in the schlieren photographs of the exhaust plume (see Figs. 20 and 21). As was the case for the 10° conical nozzle, shock waves are apparently generated by discontinuities of the second derivative of the nozzle contour at the throat. Traces of a second shock surface are evident in the schlieren photographs. This shock wave is formed by the coalescence of the compression waves generated at the inflection of the contoured nozzle's divergent section.

Numerical solutions generated using a method-of-characteristics code like that described in Reference 5 (termed the "Theoretical-MIRADCOM") indicate the formation of this shock surface (Ref. 13). Although the numerical solution generated at MIRADCOM handles only one internal shock wave, the solution depicts waves coalescing along a

curve which corresponds closely to the photographic trace of the shock wave. This recompression shock develops even though the radius of curvature of the divergent section is very large, i.e., the nozzle wall is nearly linear, as evident in Fig. 5(c) in which the nozzle is shown five times larger than full scale.

Because of the multiple shocks present in the plume, the flow is obviously nonisentropic. Therefore, method-of-characteristics solutions were not generated for the exhaust plume from this nozzle. The experimental distributions are compared in Fig. 20 with those obtained for the 10° conical nozzle. For $\tilde{x} \leq 2.0 r_{ne}$, the pitot-pressure distributions are essentially the same at the radial locations outside the shock waves. The differences in the number, locations, and strengths of the shock waves through which the flow passes produces marked differences in the pitot-pressure distributions near the axis of symmetry. The pitot-pressure distributions measured at $\tilde{x} = 3.0 r_{ne}$ are the same for both nozzles across the entire plume. Thus, the effects of the internal shock waves are washed out by the streamwise acceleration of the flow in the expanding plume.

A Comparison of the Plume Boundaries

The theoretical and the experimental plume boundaries for the 20° conical nozzle with $p_{t1} = 8.715 \times 10^6 \text{ N/m}^2$ (1264 psia) are compared in Fig. 22. Since these data are for the highest Reynolds number flow, turbulence affects the shear layer thickness, as indicated in Fig. 12. Furthermore, of the three nozzles tested, the

correlation between theory and experiment is poorest for this nozzle (which has the largest nozzle exit-angle). As noted earlier, the plume boundary computed using the RMOC code lies slightly nearer to the actual boundary than that computed using the MOC code. This is true even though the RMOC code in its present form does not suitably describe the expansion process.

The theoretical and the experimental plume boundaries for the two nozzle configurations for which $\theta_{ne} = 10^\circ$ are presented in Fig. 23. In addition to the solution for the 10° conical nozzle which was generated using the University's MOC code, solutions were obtained for both nozzles using a MIRADCOM code (Ref. 13). The equations used in the MIRADCOM code are similar to those used in the University's RMOC code. Starting from a plane of information just downstream of the throat, the MIRADCOM solutions represent the flow in the divergent section of the nozzle and in the free plume. A nozzle-wall boundary layer is included in the flow model. Note that the MIRADCOM solutions presented in Fig. 23 for the 10° contoured nozzle did not model the internal shock wave. The internal shock wave was not represented since the MIRADCOM code can handle only one shock wave in the flow field and the boundary shock wave was "encountered" first in the solution procedure. The flow field solution did have closely spaced characteristics where the compression waves coalesce to form a shock wave. Despite the failure to include all of the internal shock waves, the correlation between the MIRADCOM solutions and the data is considered excellent. Note that the plume boundary for the contoured nozzle lies beyond that for the conical

nozzle, both experimentally and theoretically.

A summary of the comparisons between the experimental and the theoretical plume boundaries is presented in Fig. 24. The data indicate that the nozzle contour and the nozzle half-angle have a significant effect on the plume boundary. Since the experimental results presented in Fig. 24 represent only one stagnation pressure and only three nozzle configurations, the reader is cautioned against drawing too general conclusions from these data. However, the data themselves and their correlation (or lack thereof) with the various method-of-characteristics codes provide valuable information for the development of an exhaust flow code.

CONCLUDING REMARKS

An experimental program has been conducted to define the exhaust plume which results when an underexpanded, supersonic stream exhausts into quiescent air. Pitot-pressure distributions and schlieren photographs were used to define the exhaust plumes for three different nozzle configurations. These experimentally-determined flow fields have been compared with the theoretical solutions generated using numerical codes based on the method of characteristics. Based on the data and their correlations with theory, the following conclusions are made.

- 1) Although the radius of curvature of the throat wall was equal to the cross-section radius of the throat, weak throat shock-waves were generated for two of the three nozzles. In addition, the compression waves generated at the inflection of the one contoured nozzle produced an additional shock wave.
- 2) These shock waves had a significant effect on the experimental pitot-pressure distributions for $\tilde{x} \leq 2.0 r_{ne}$. By $\tilde{x} = 3.5 r_{ne}$, the streamwise acceleration of the flow in the expanding plume washed out the effects of the nozzle shock waves.
- 3) The plume boundaries did not appear to be significantly affected by the internal shock waves. As expected, the plume boundary depended on the stagnation pressure and the nozzle angle at the exit plane. It also depended on the geometry of the divergent section. With $\theta_{ne} = 10^\circ$, the plume boundary for the contoured

nozzle was outside that for the conical nozzle, both theoretically and experimentally.

- 4) The nondimensionalized distance between the actual plume boundary and the plume boundary computed using the MOC code changed "discontinuously" as the stagnation pressure (or the Reynolds number) increased above a critical value. The change was attributed to the onset of transition.

REFERENCES

1. E.S. Love, C.E. Grigsby, L.P. Lee, and M.J. Woodling, "Experimental and Theoretical Studies of Axisymmetric Free Jets", TR R-6, 1959, NASA.
2. M. Pindzola, "Jet Simulation in Ground Test Facilities," AGARDograph 79, Nov. 1963, NATO Advisory Group for Aeronautical Research and Development.
3. R.D. Herron, "Investigation of Jet Boundary Simulation Parameters for Underexpanded Jets in a Quiescent Atmosphere", AEDC-TR-68-108, September 1968, Arnold Engineering Development Center.
4. H.H. Korst, "Approximate Determination of Jet Contours Near the Exit of Axially Symmetric Nozzles as a Basis for Plume Modeling", Technical Report No. RD-72-14, August 1972, Aeroballistics Directorate, U.S. Army Missile Command.
5. R.J. Prozan, "Solution of Non-isoenergetic Supersonic Flows by Methods of Characteristics", LMSC-HREC D16 2220-III, July 1971, Lockheed Missiles and Space Company, Huntsville, Alabama.
6. L.H. Back and R.F. Cuffel, "Detection of Oblique Shocks in a Conical Nozzle with a Circular-Arc Throat", AIAA Journal, December 1966, Vol. 4, No. 12, pp. 2219-2221.
7. J. Leng, C.W. Osonitsch, and T.M. Lacinski, "Effects of Oblique Shock Waves in the Near Field of Rocket Plumes", Journal of Spacecraft and Rockets, November 1969, Vol. 6, No. 11, pp. 1316-1319.
8. _____: "Equations, Tables, and Charts for Compressible Flow", Report 1135, 1953, NACA.
9. Hartree, D.R., Numerical Analysis, 1958, Clarendon Press, Oxford, England.
10. J.J. Bertin, S.J. Sutter, D.P. Dannemiller, and D.L. Booker, "Comparison of Theoretical and Experimental Flow Fields for an Underexpanded Rocket Exhaust", AIAA Paper 79-0340, presented at the AIAA 17th Aerospace Sciences Meeting, New Orleans, January 1979.
11. Bartlett, E.P. and Kendall, R.M., "An Analysis of the Coupled Chemically Reacting Boundary Layer and Charring Ablator, Part III, Nonsimilar Solution of the Multicomponent Laminar Boundary Layer by an Integral Matrix Method", NASA CR-1062, June 1968.

12. J.J. Bertin, H.T. Faria, W.D. Goodrich, and W.R. Martindale, "Effect of Nose Geometry on the Aerothermodynamic Environment of Shuttle Entry Configurations", Journal of Spacecraft and Rockets, May 1974, Vol. 11, pp. 275-281.
13. Private transmittal from D.L. Booker, U.S. Army Missile Research and Development Command, 4 December 1978.

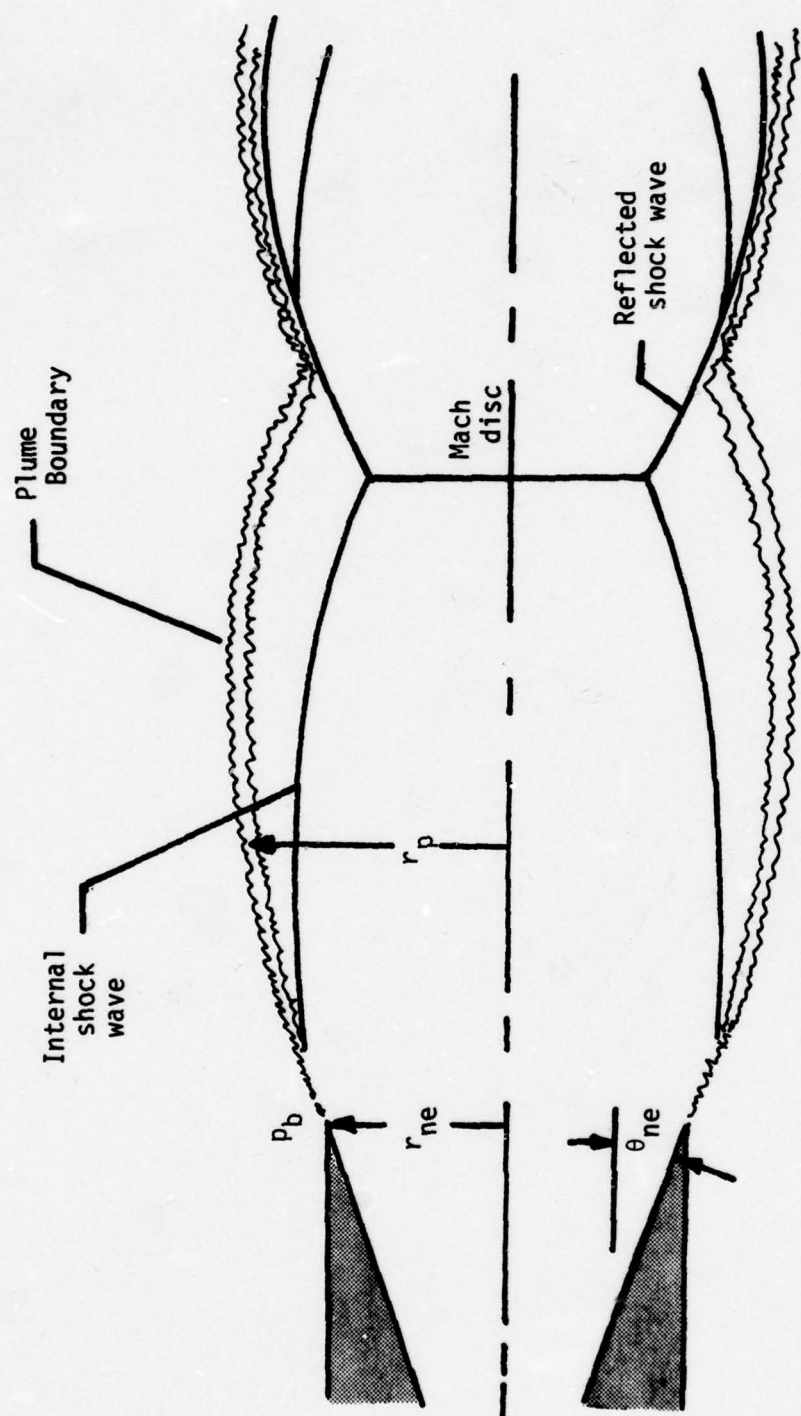


Figure 1. - Sketch of generalized flow pattern of an underexpanded, axisymmetric jet exhausting into a static medium.

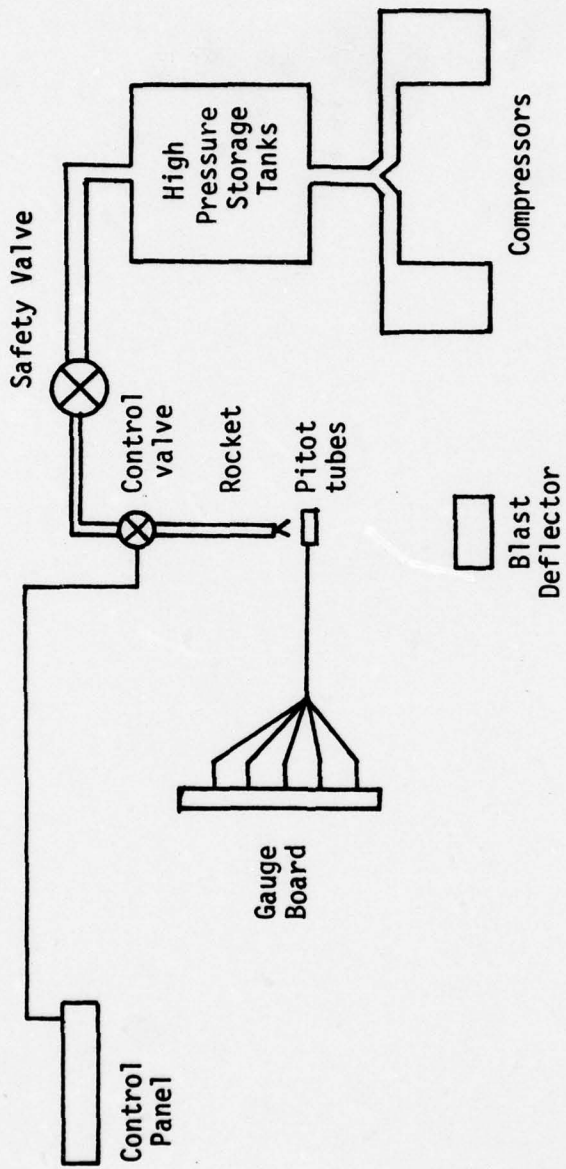


Figure 2. - Schematic of the University of Texas Rocket Exhaust Effects Facility

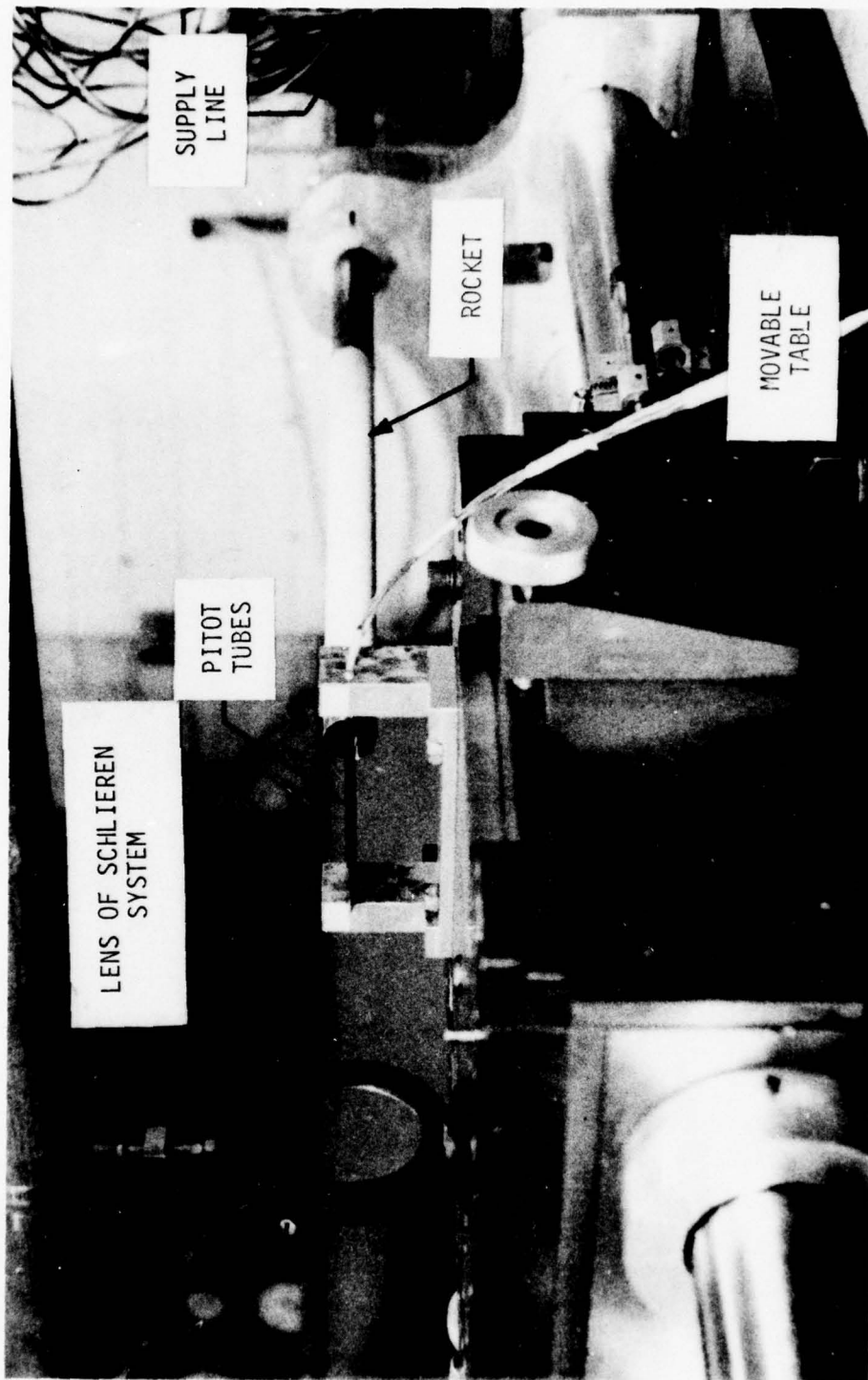


Figure 3. The Rocket Exhaust Effects Facility

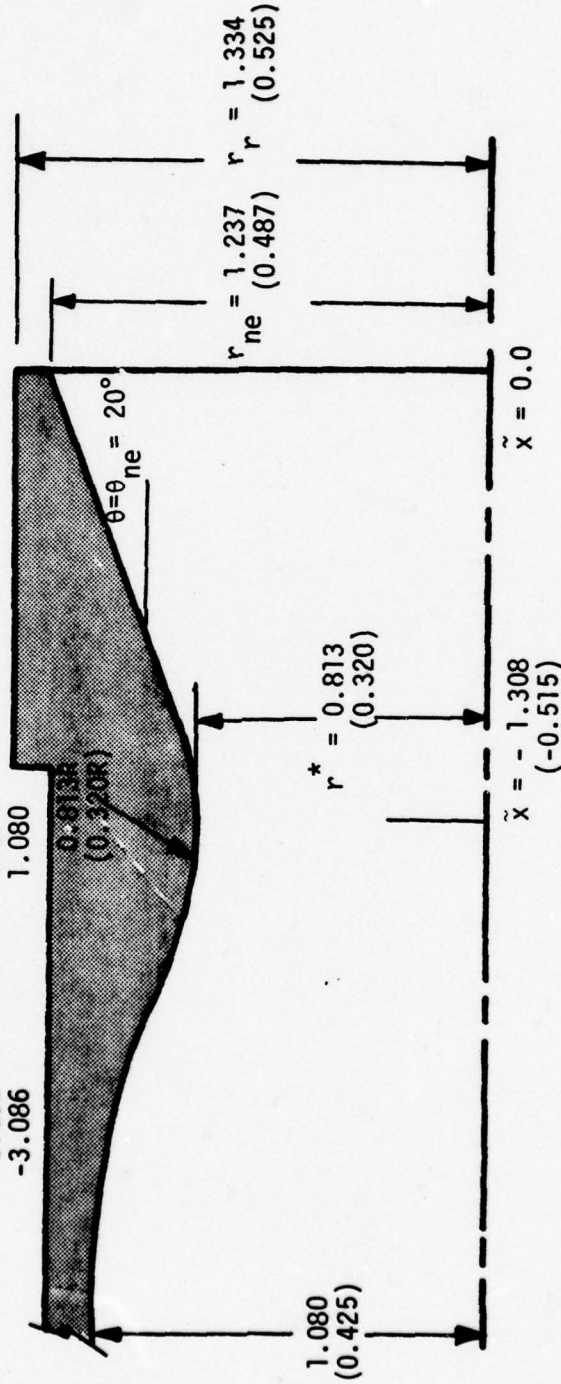
Convergent Section: $\tilde{x} < -1.308$

\tilde{x} (cm)	r (cm)
-1.562	0.856
-1.816	0.937
-2.070	1.006
-2.324	1.049
-2.578	1.064
-2.832	1.074
-3.086	1.080

Equations for Divergent Section (cm):

For $-1.308 \leq \tilde{x} \leq -1.031$
 $(\tilde{x} + 1.308)^2 + (r - 1.626)^2 = (0.813)^2$

For $-1.031 \leq \tilde{x} \leq 0.0$
 $r = 0.759 + 0.364 (\tilde{x} + 1.308)$



(a) 20° Conical Nozzle

Figure 4. - Sketches of the nozzle configurations. Note, the dimensions are given in cm(in.).

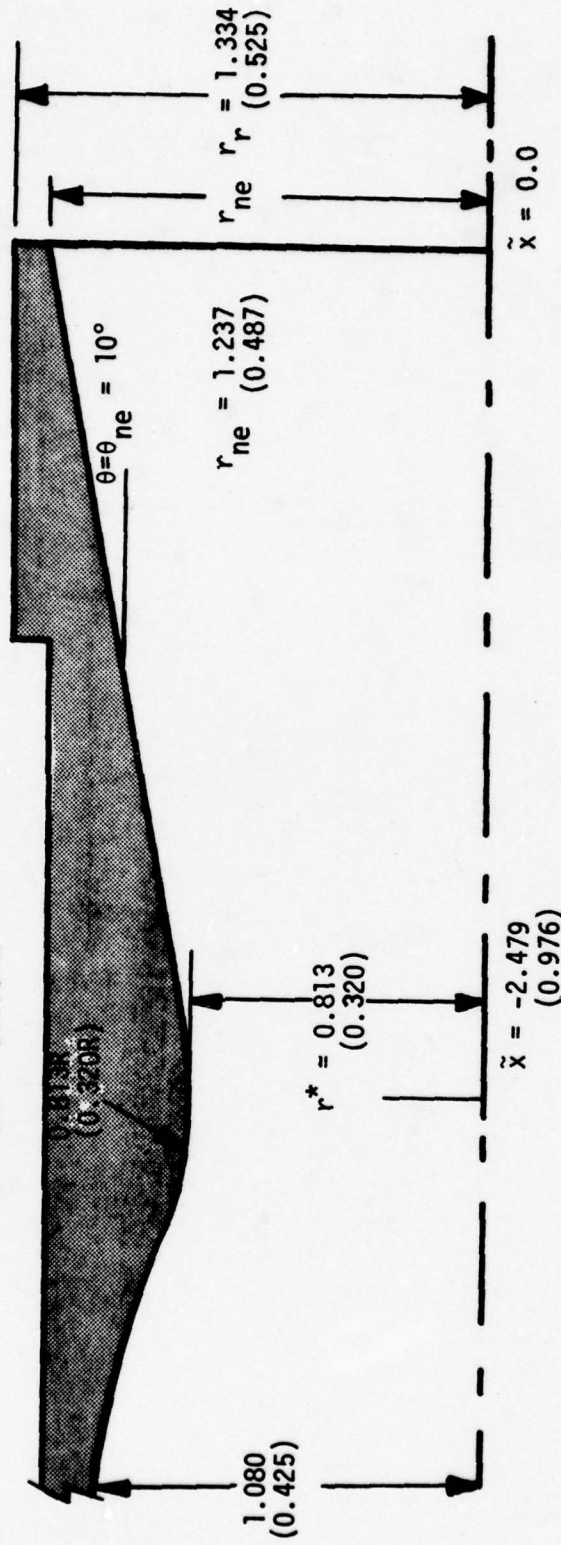
Equations for Divergent Section (cm):

For $-2.479 \leq \tilde{x} \leq -2.338$

$$(\tilde{x} + 2.479)^2 + (r - 1.626)^2 = (0.813)^2$$

For $-2.338 < \tilde{x} \leq 0.0$

$$r - 1.237 = 0.176 \tilde{x}$$



(b) 10° Conical Nozzle

Figure 4. - Continued

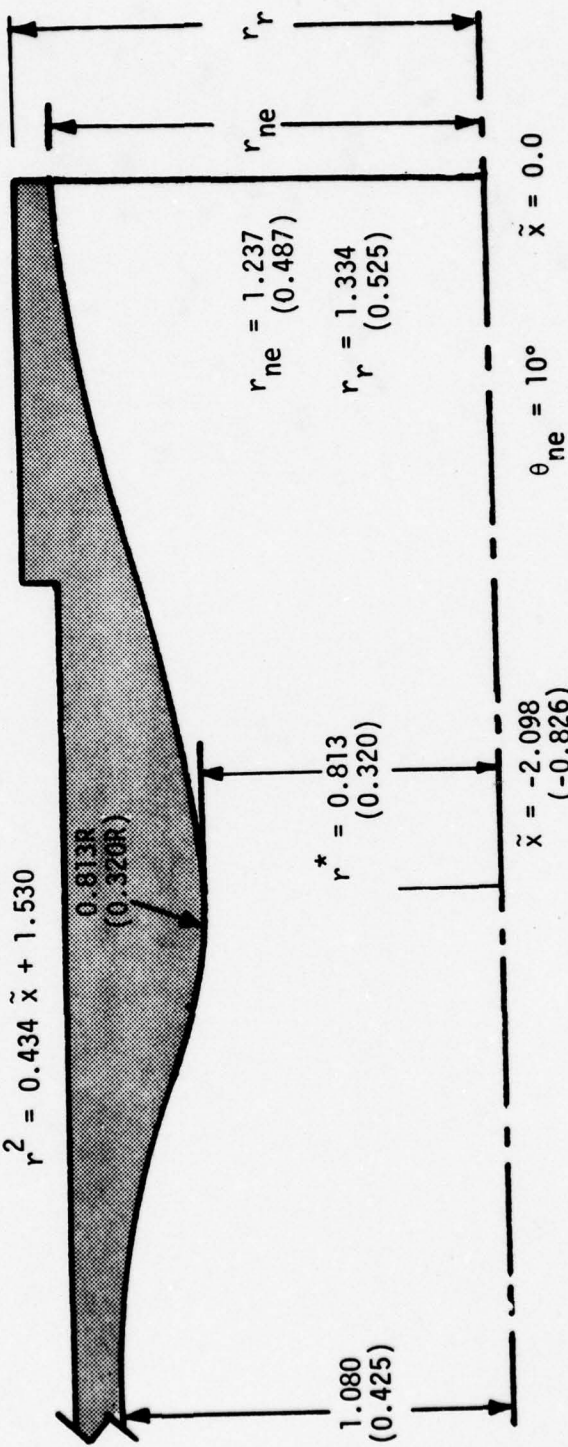
Equations for Divergent Section (cm):

For $-2.908 \leq \tilde{x} \leq -1.895$

$$(\tilde{x} + 2.098)^2 + (r - 1.676)^2 = (0.813)^2$$

For $-1.895 < \tilde{x} \leq 0.0$

$$r^2 = 0.434 \tilde{x} + 1.530$$



(c) 10° Contoured Nozzle

Figure 4. - Concluded

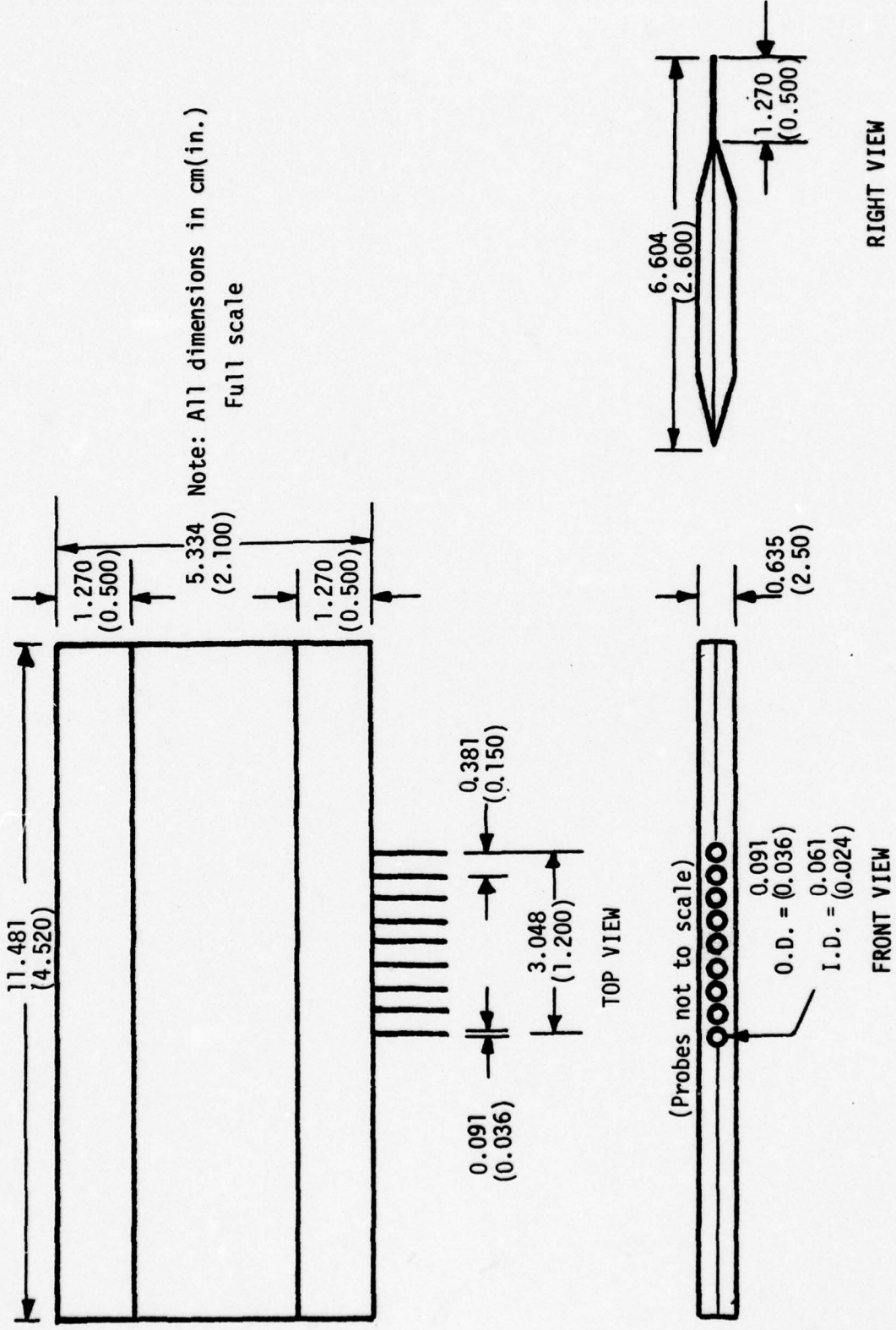


Figure 5. - Sketch of pitot probe assembly

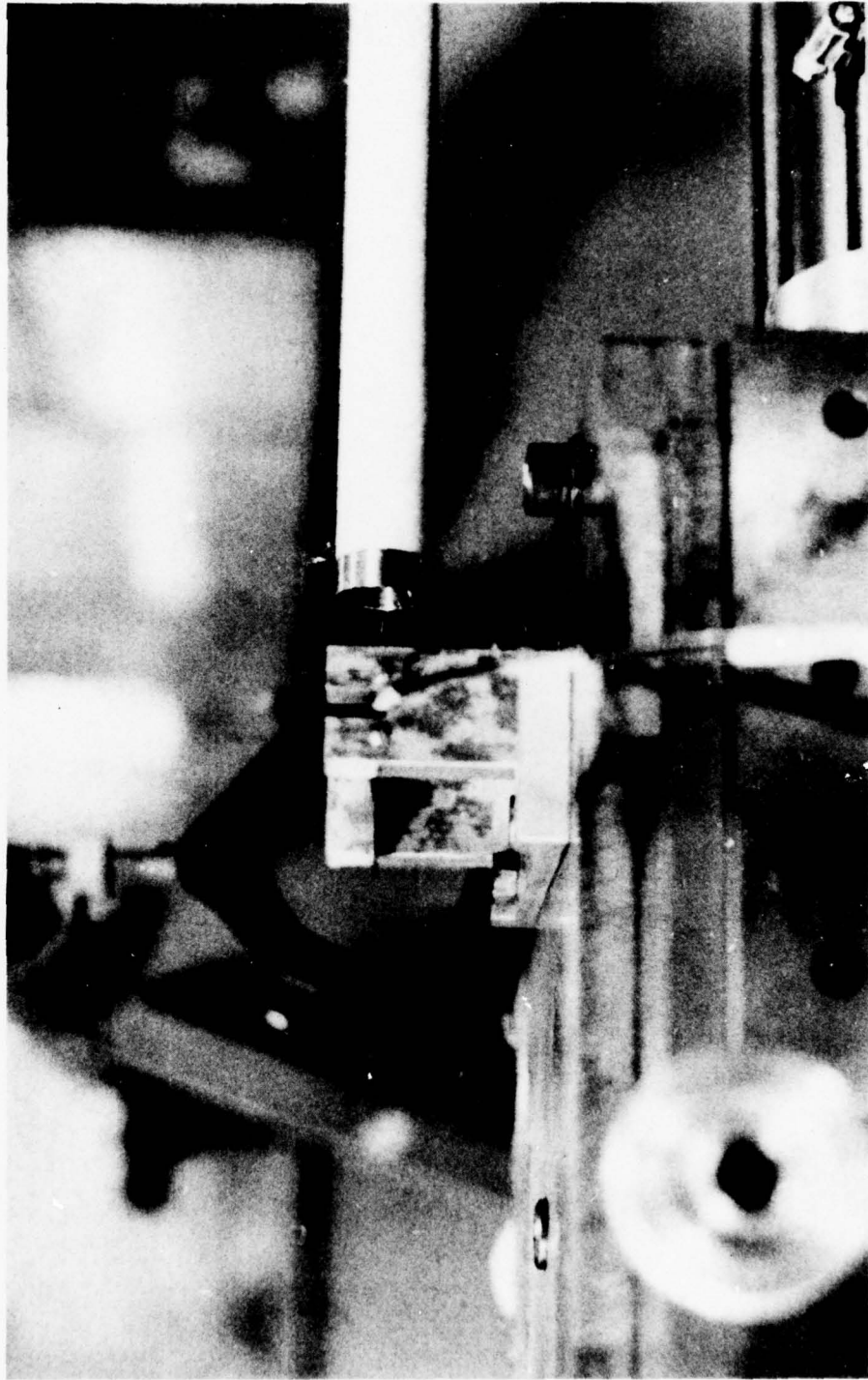


Figure 6. Pitot probe assembly mounted on the movable table

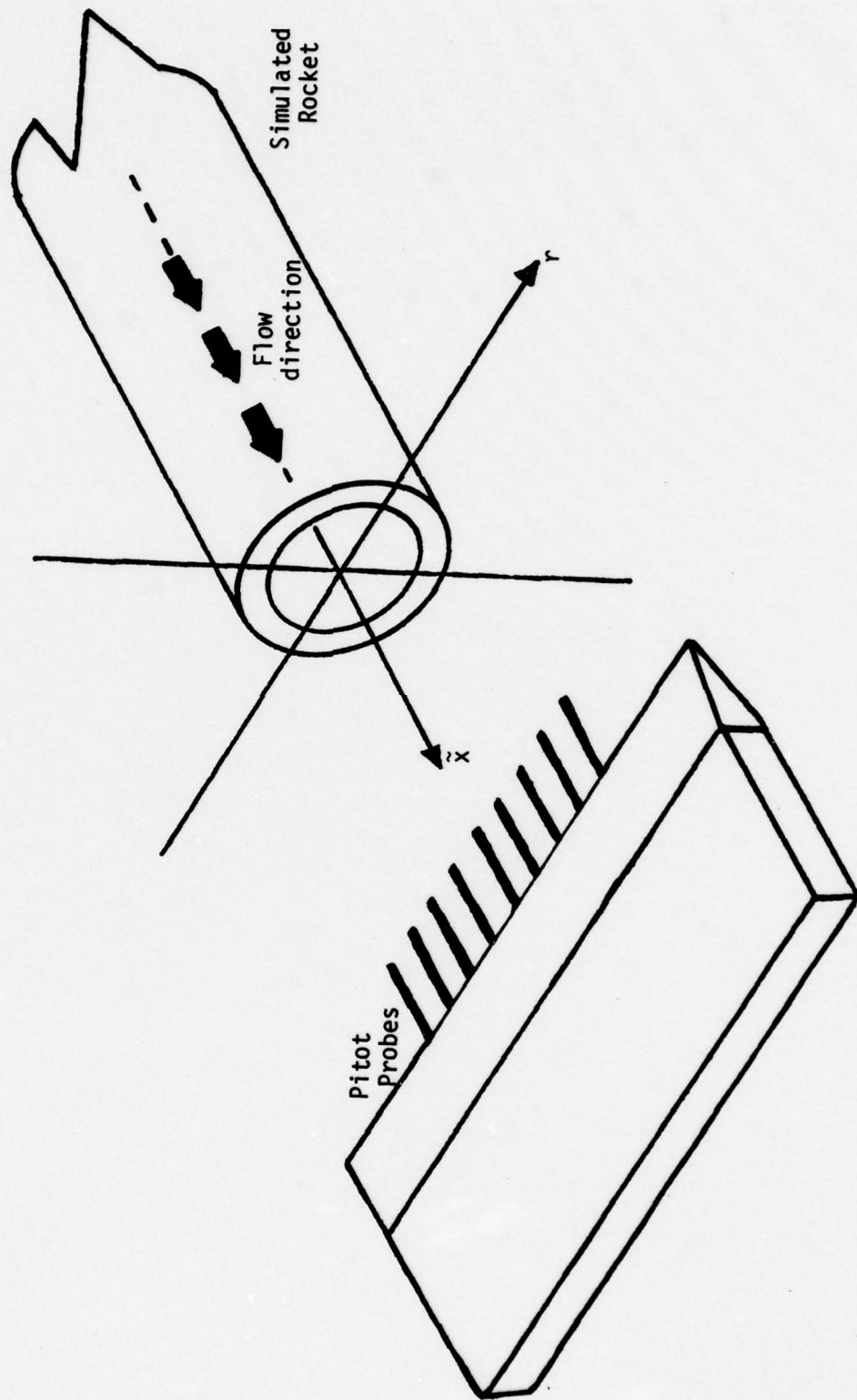


Figure 7. - Simulated rocket nozzle exit-plane oriented coordinate system

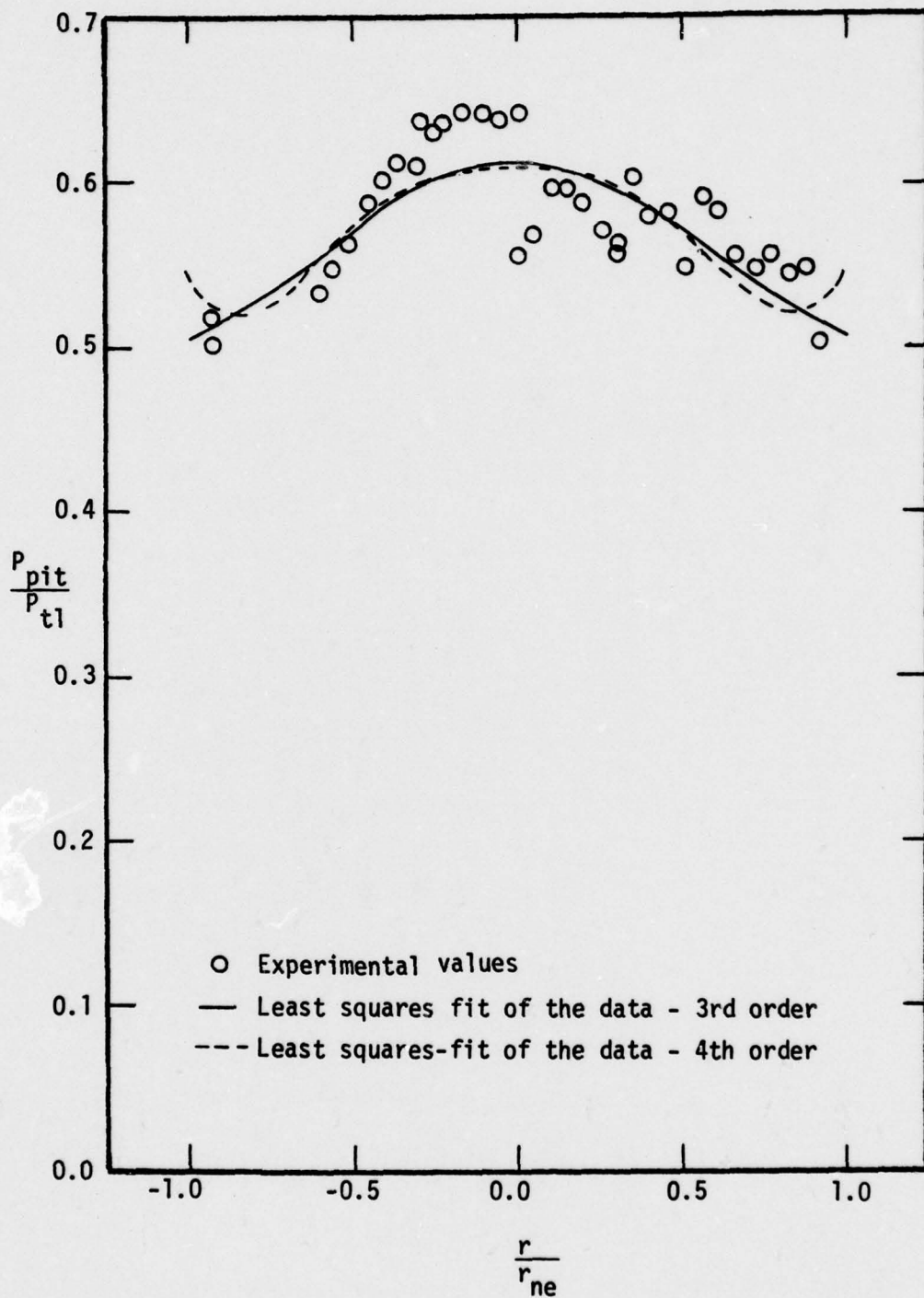


Figure 8. Pitot-pressure distribution for the nozzle exit-plane of 20° conical nozzle, $P_{t1} = 8.715 \times 10^6 \text{ N/m}^2$ (1264 psia)

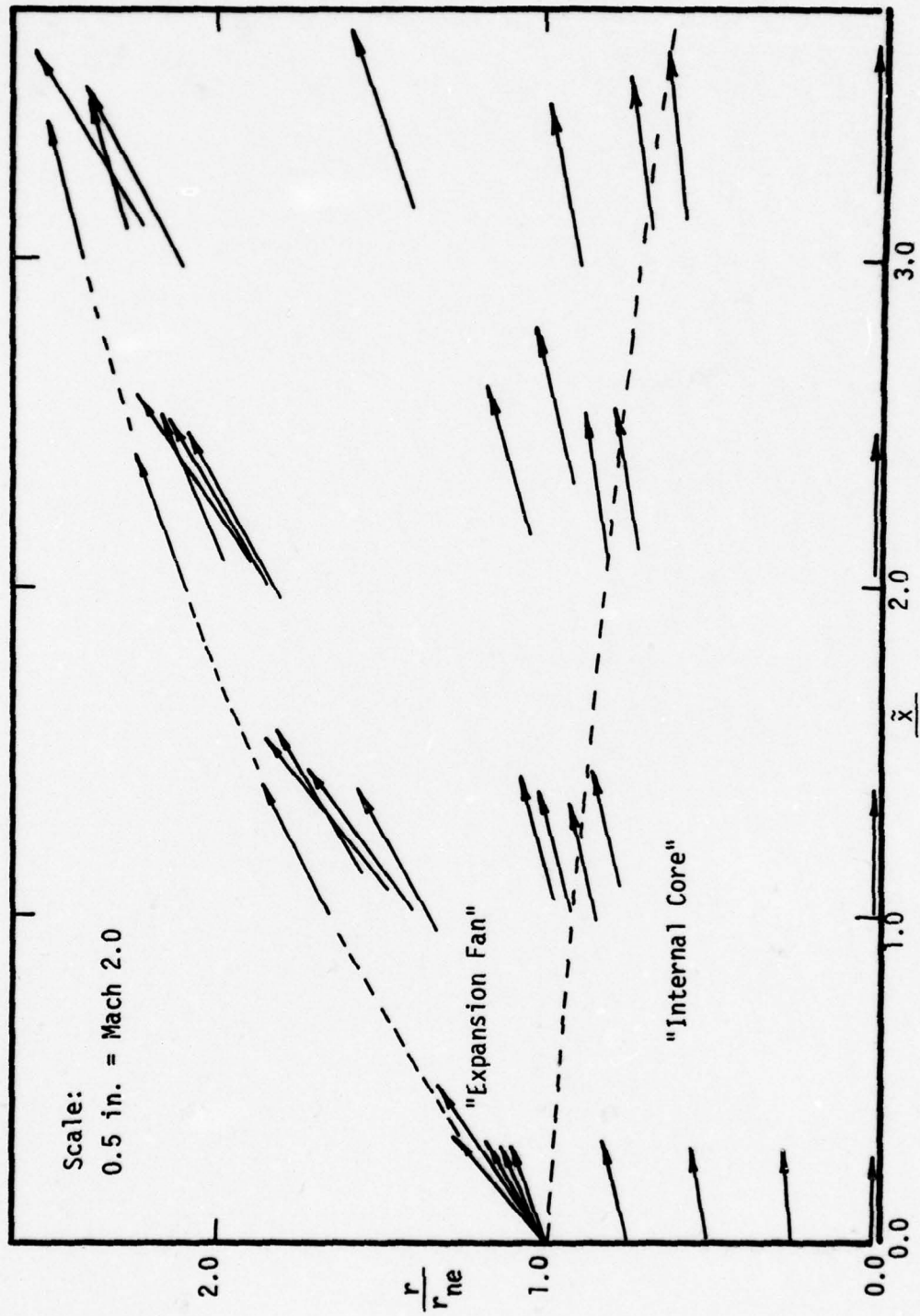


Figure 9. - Theoretical Mach numbers and flow directions of 20° conical nozzle, $P_{tj} = 8.715 \times 10^6 \text{ N/m}^2$ (1264 psia)

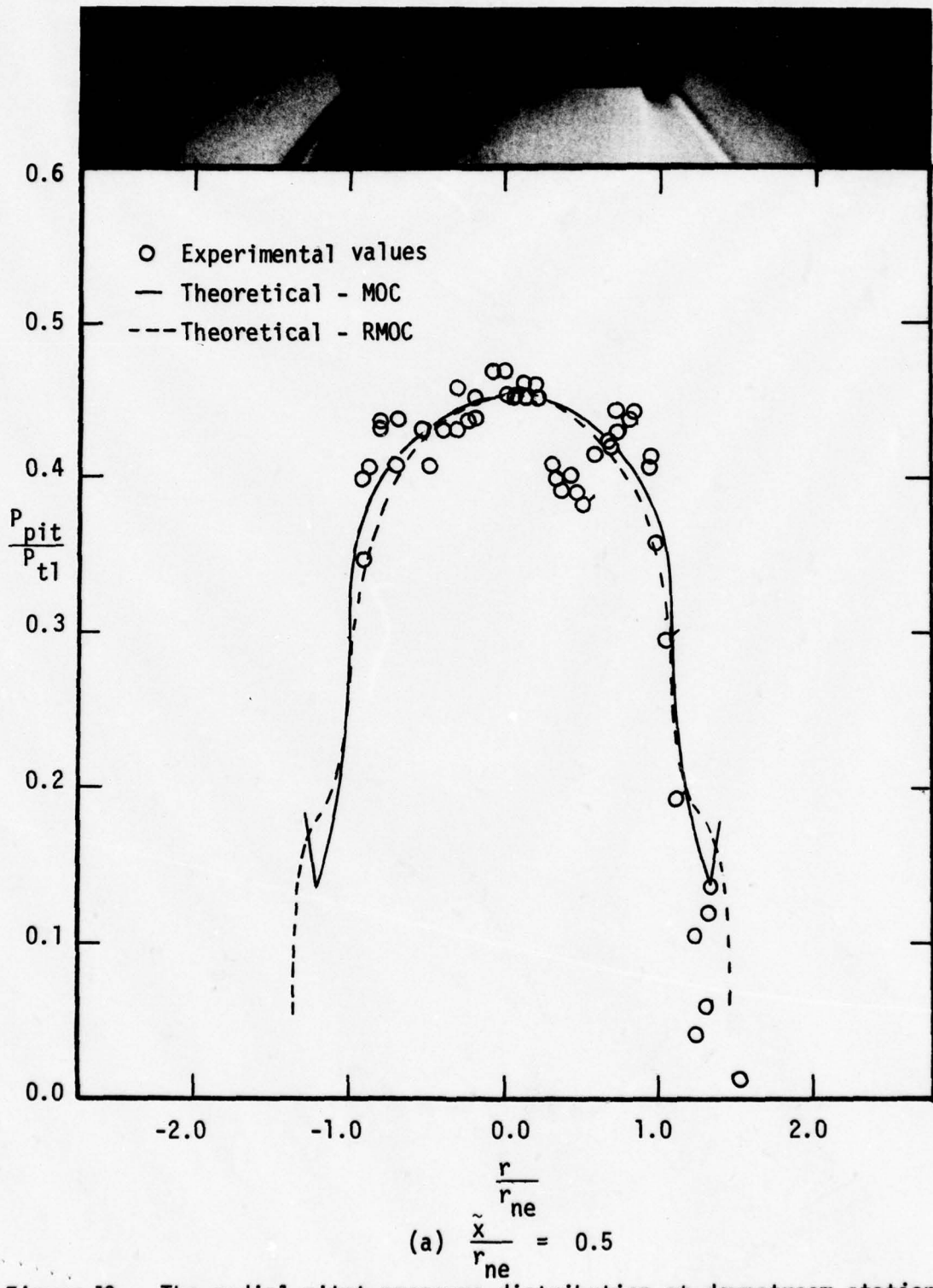
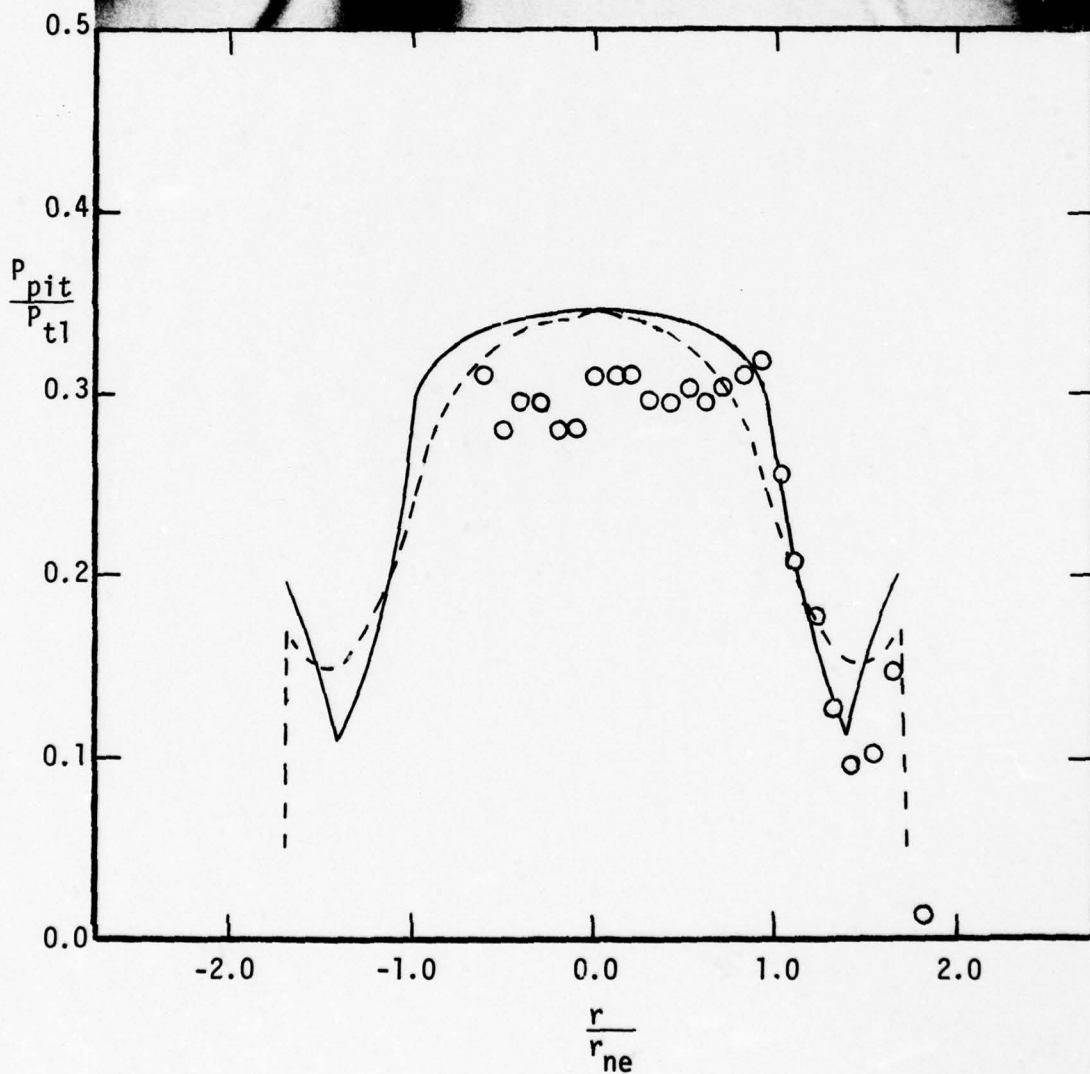
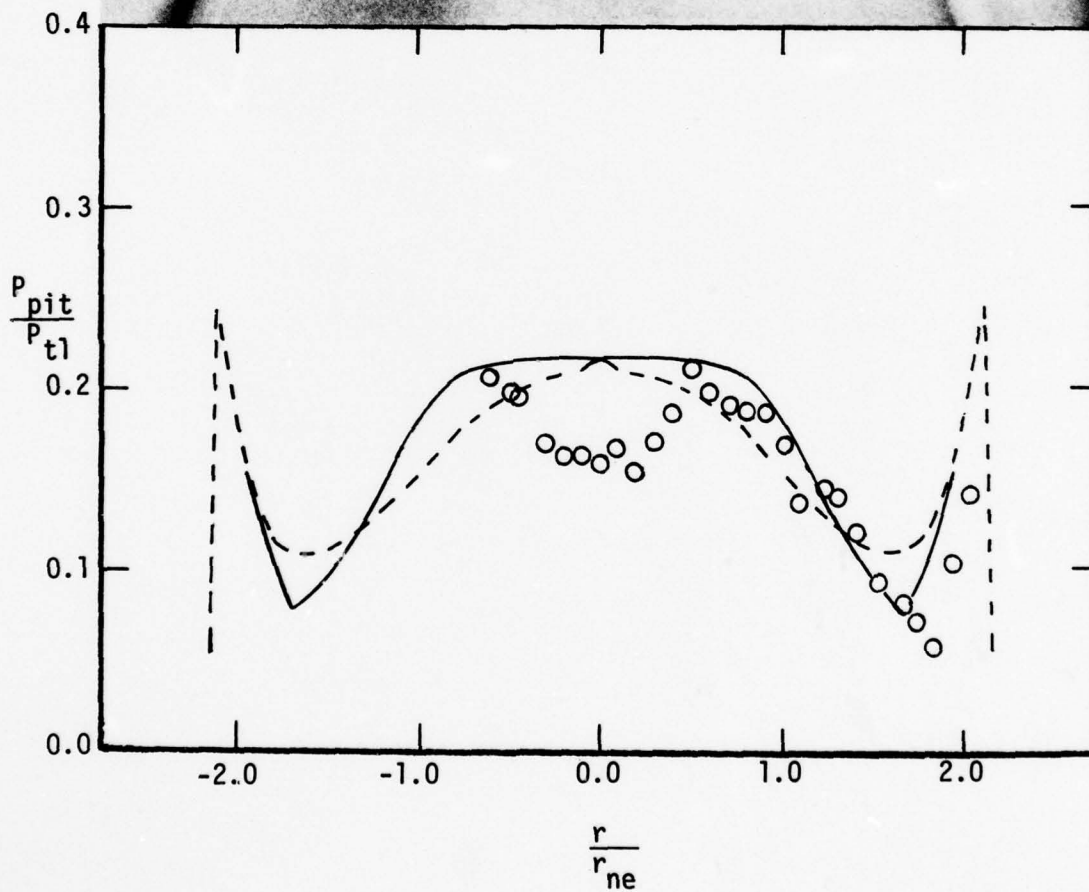
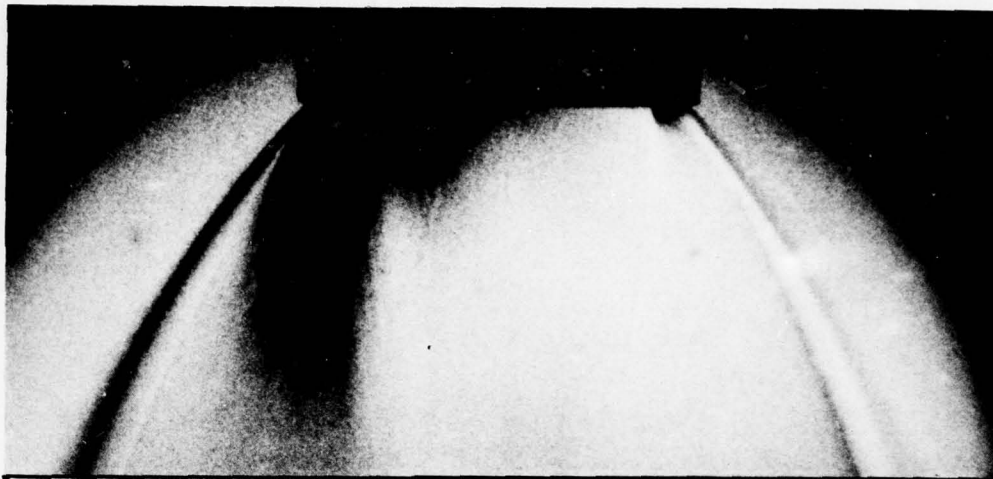


Figure 10. - The radial pitot-pressure distribution at downstream stations; 20° conical nozzle, $P_{t1} = 8.715 \times 10^6 \text{ N/m}^2$ (1264 psia)



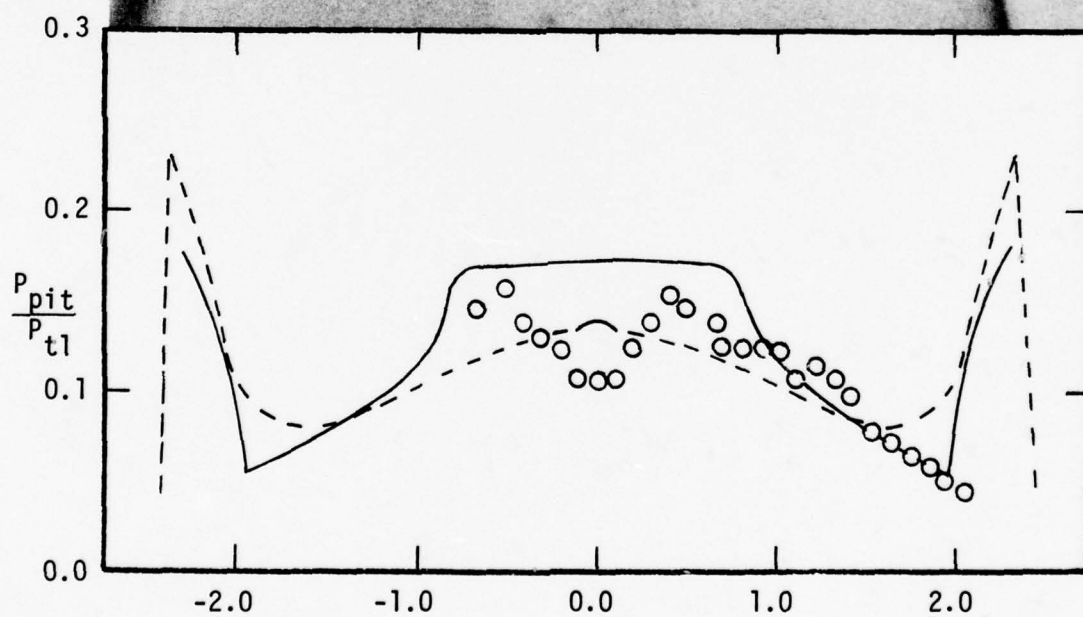
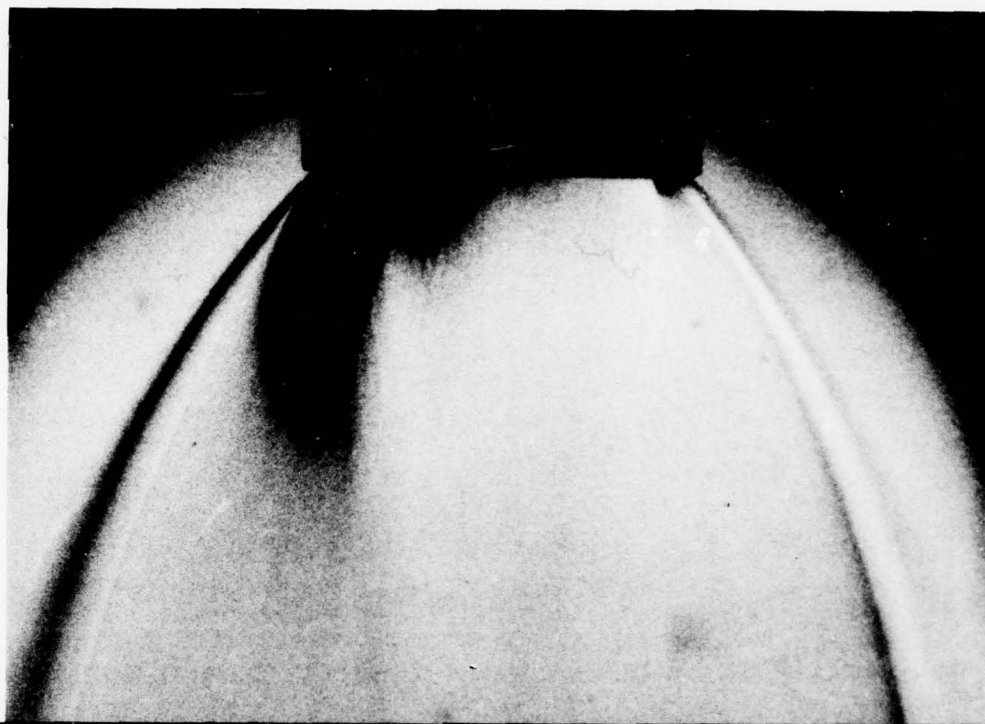
(b) $\frac{\tilde{x}}{r_{ne}} = 1.0$

Figure 10. - Continued



(c) $\frac{\tilde{x}}{r_{ne}} = 2.0$

Figure 10. - Continued



$$(d) \frac{\tilde{x}}{r_{ne}} = 3.0$$

Figure 10. - Concluded

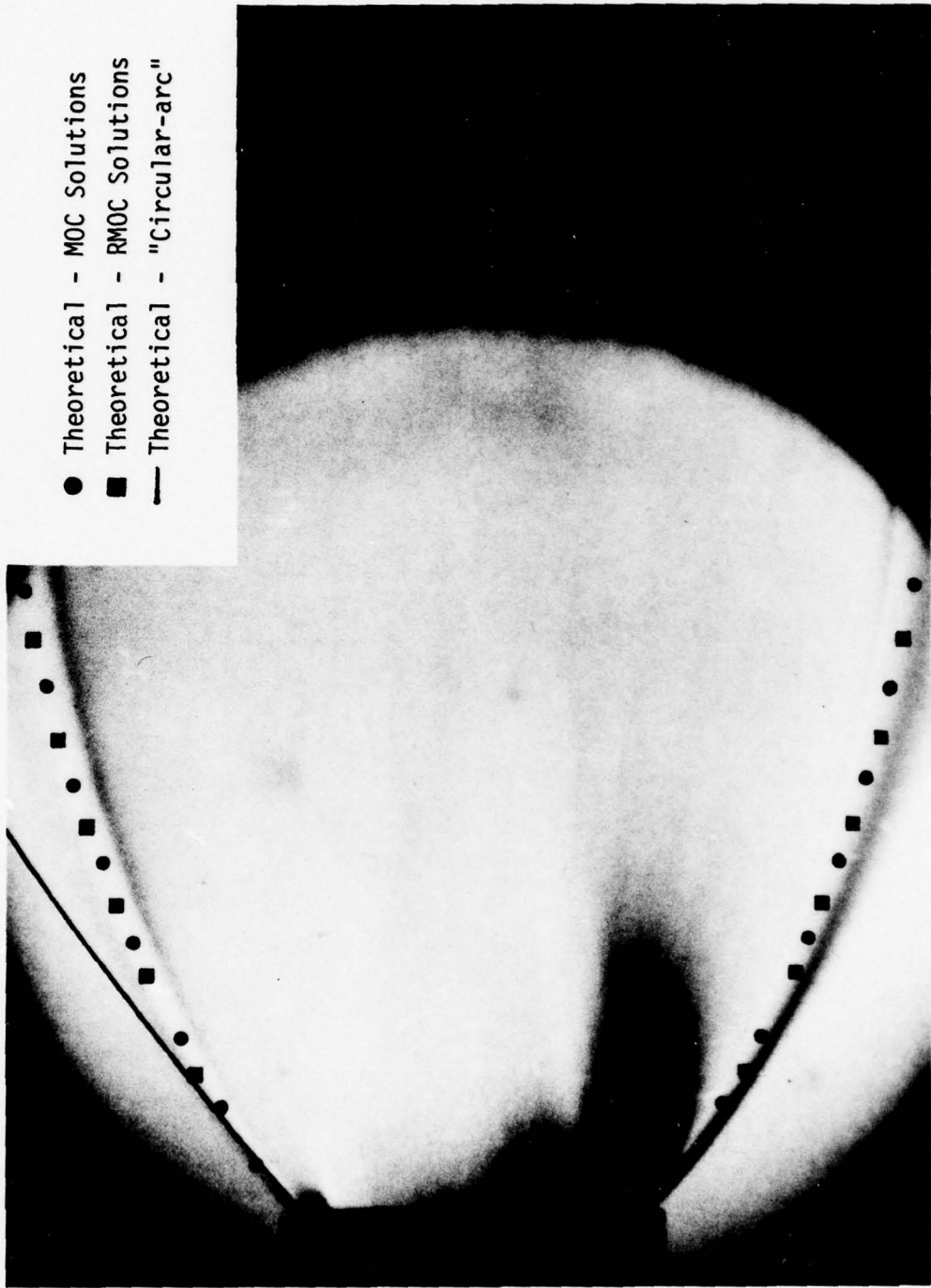


Figure 11. - Comparison of theoretical MOC and RMOC solutions with the experimental plume boundary of the 20° conical nozzle, $P_{t1} = 8.715 \times 10^6 \text{ N/m}^2 \text{ (psia)}$

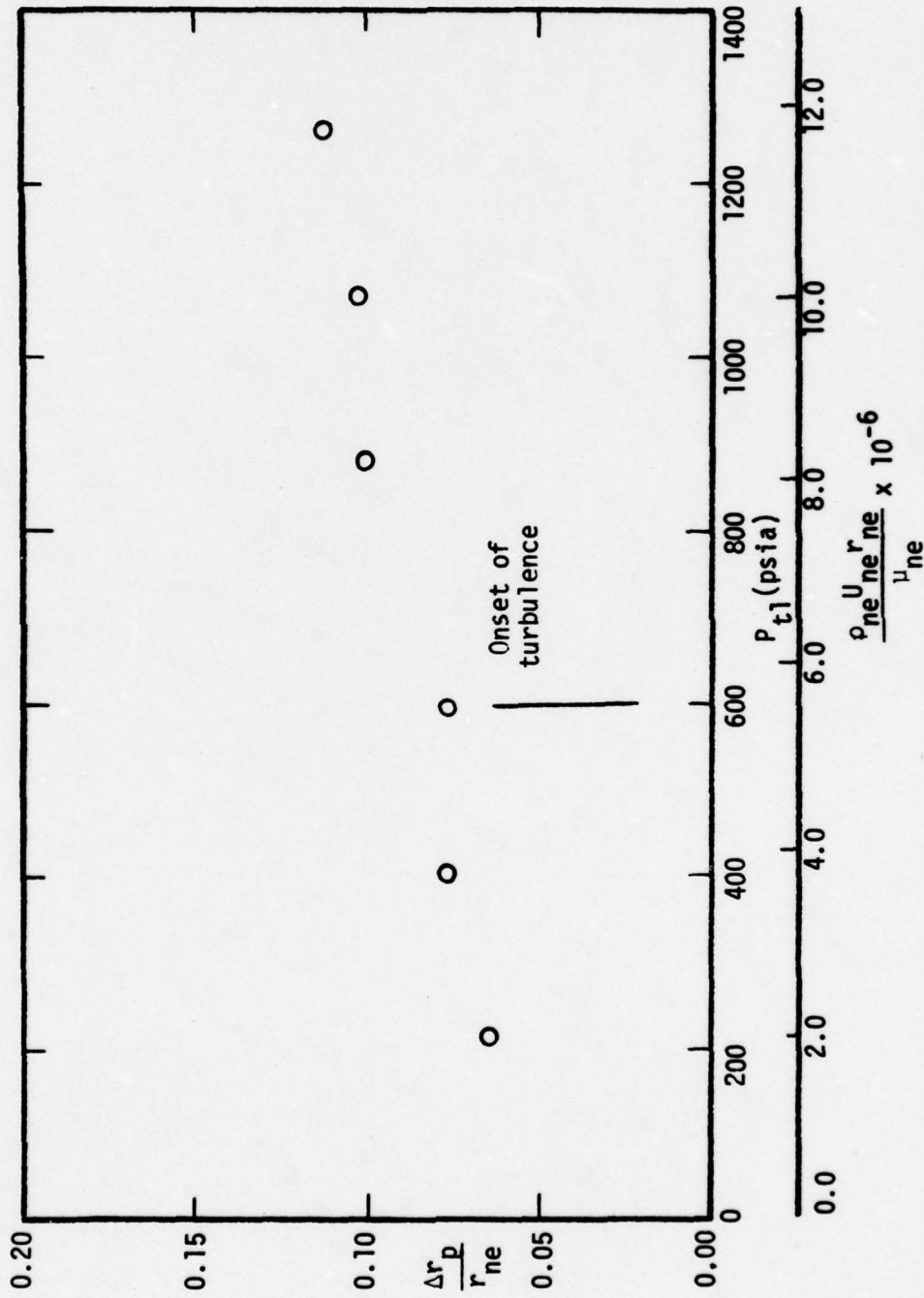


Figure 12. - Effect of the nozzle exit Reynolds Number on the location of the experimental plume boundary relative to the calculated inviscid boundary at $\tilde{x} = 1.0 r_{ne}$ for the 20° conical nozzle

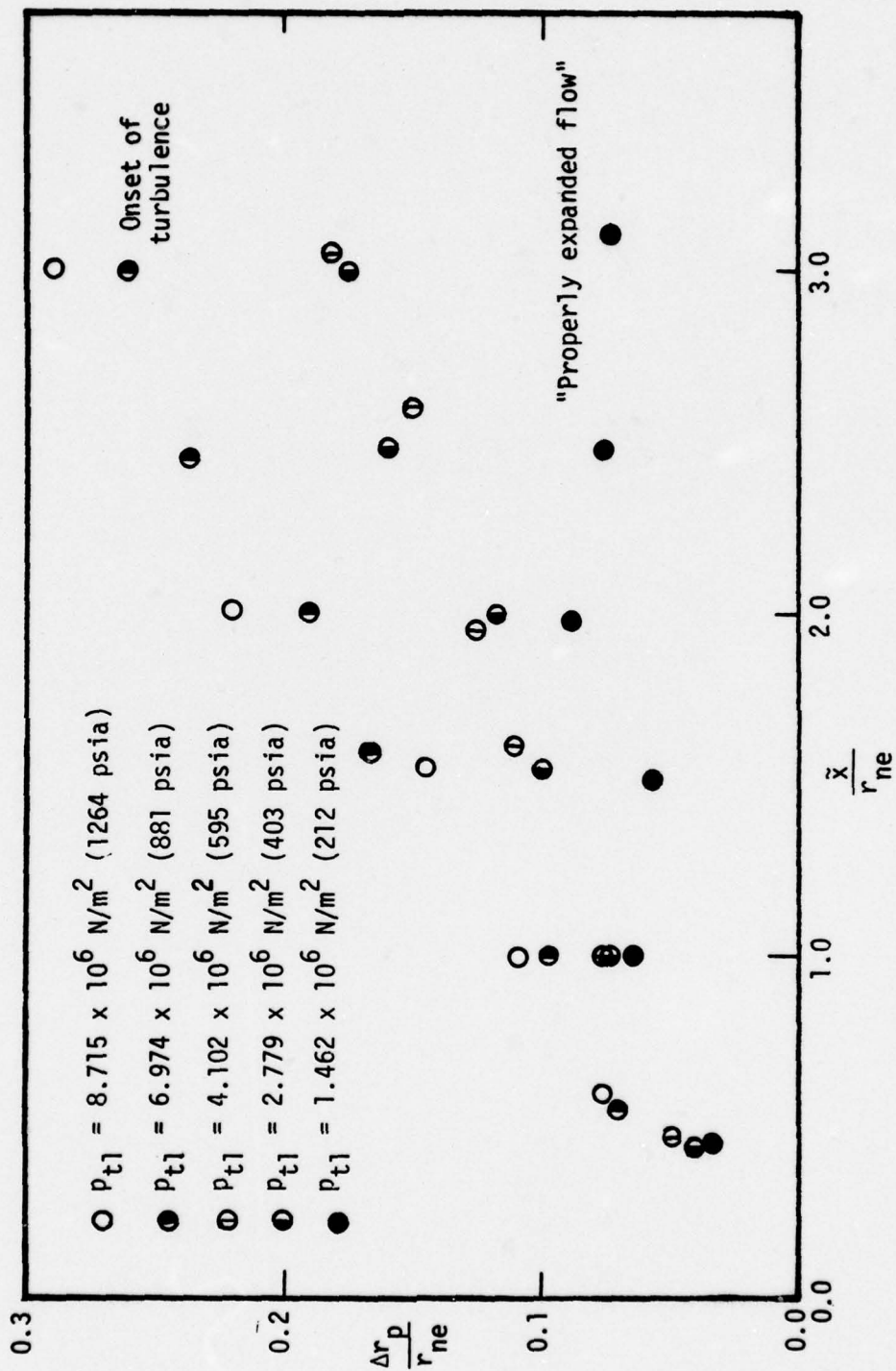


Figure 13. - Effect of stagnation pressure, P_{t1} , on the location of the experimental plume boundary relative to the calculated inviscid boundary at downstream stations for the 20° conical nozzle.

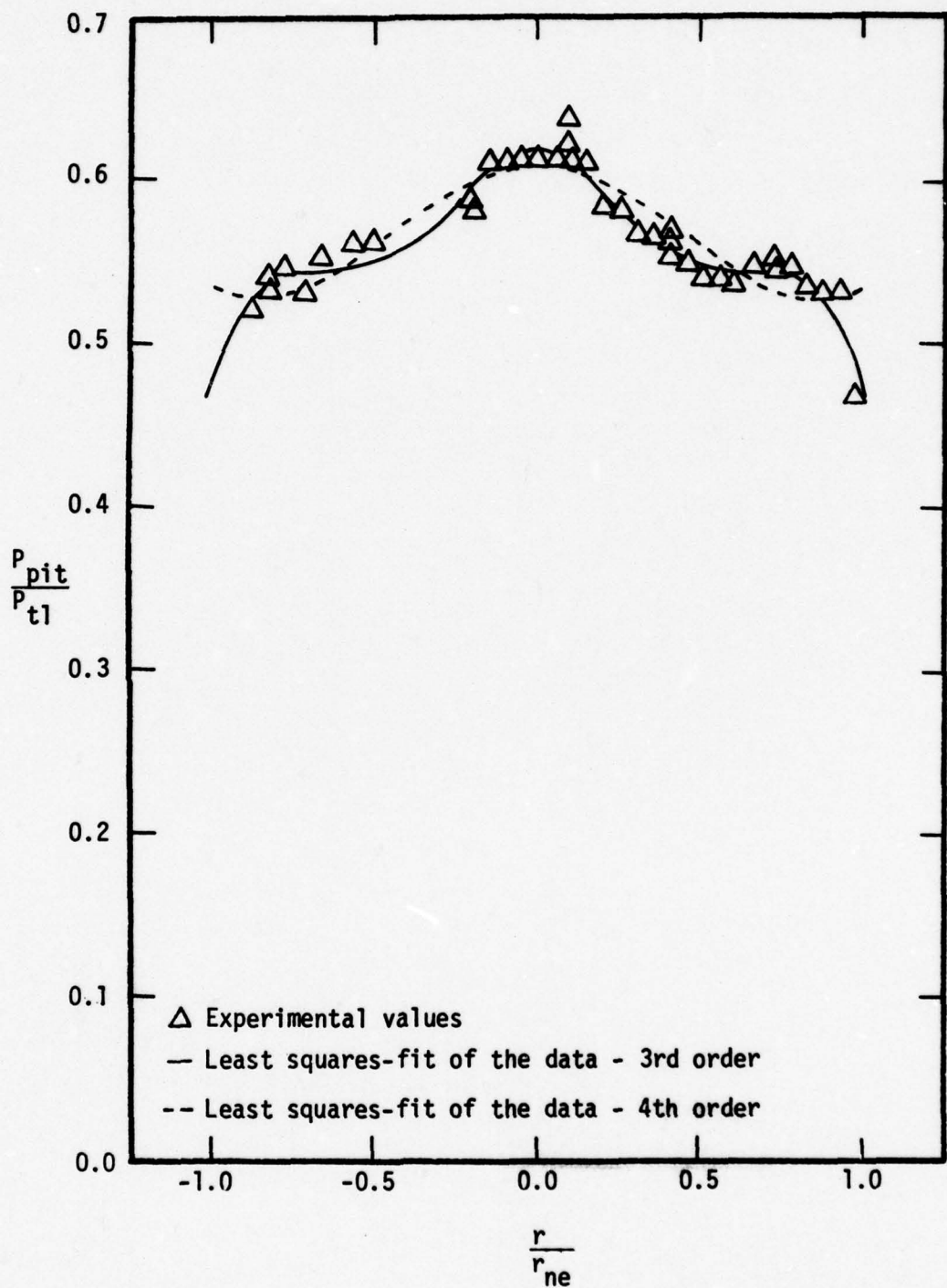


Figure 14. - Pitot-pressure distribution for the nozzle exit plane of 10° conical nozzle, $P_{t1} = 8.715 \times 10^6 \text{ N/m}^2$ (1264 psia)

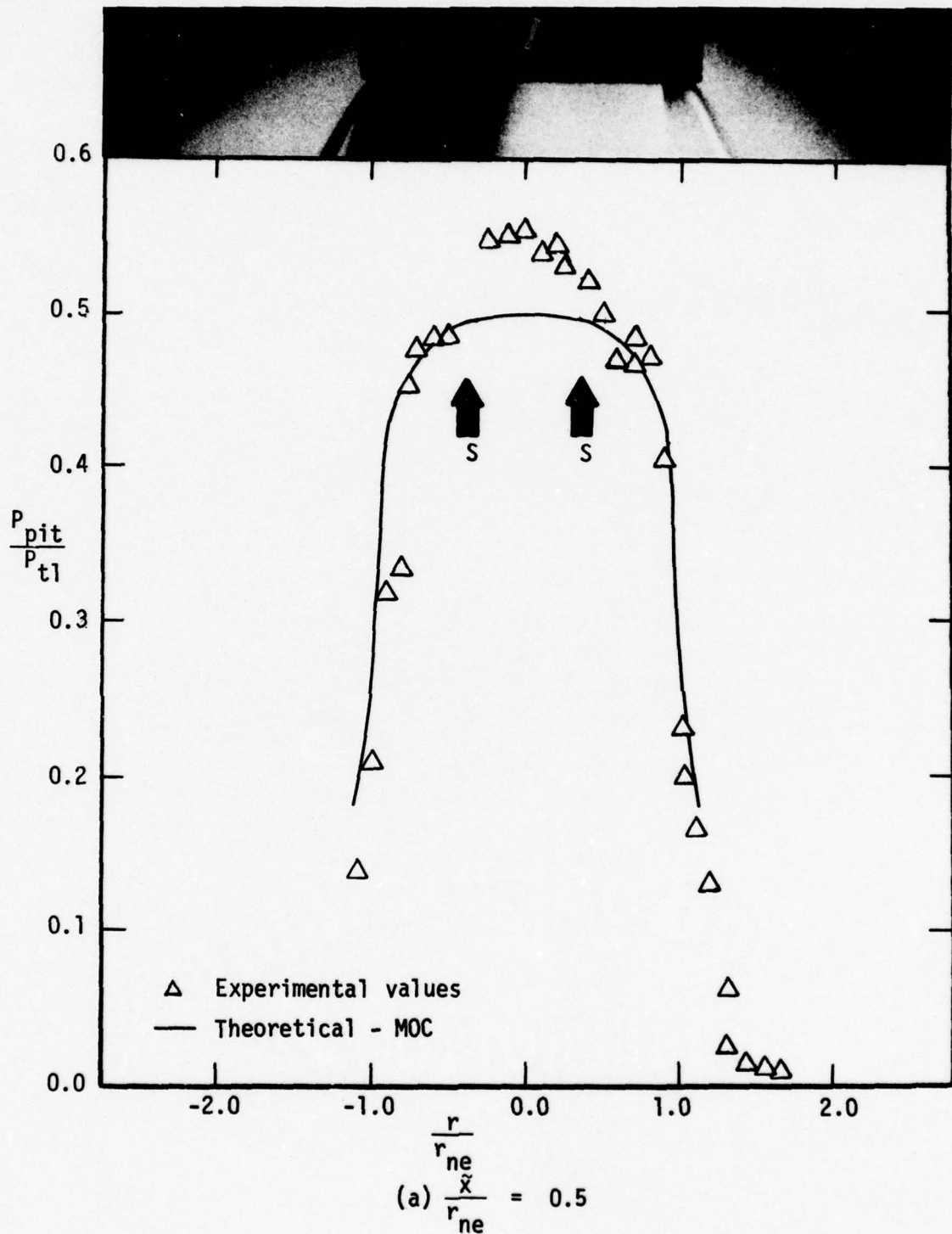
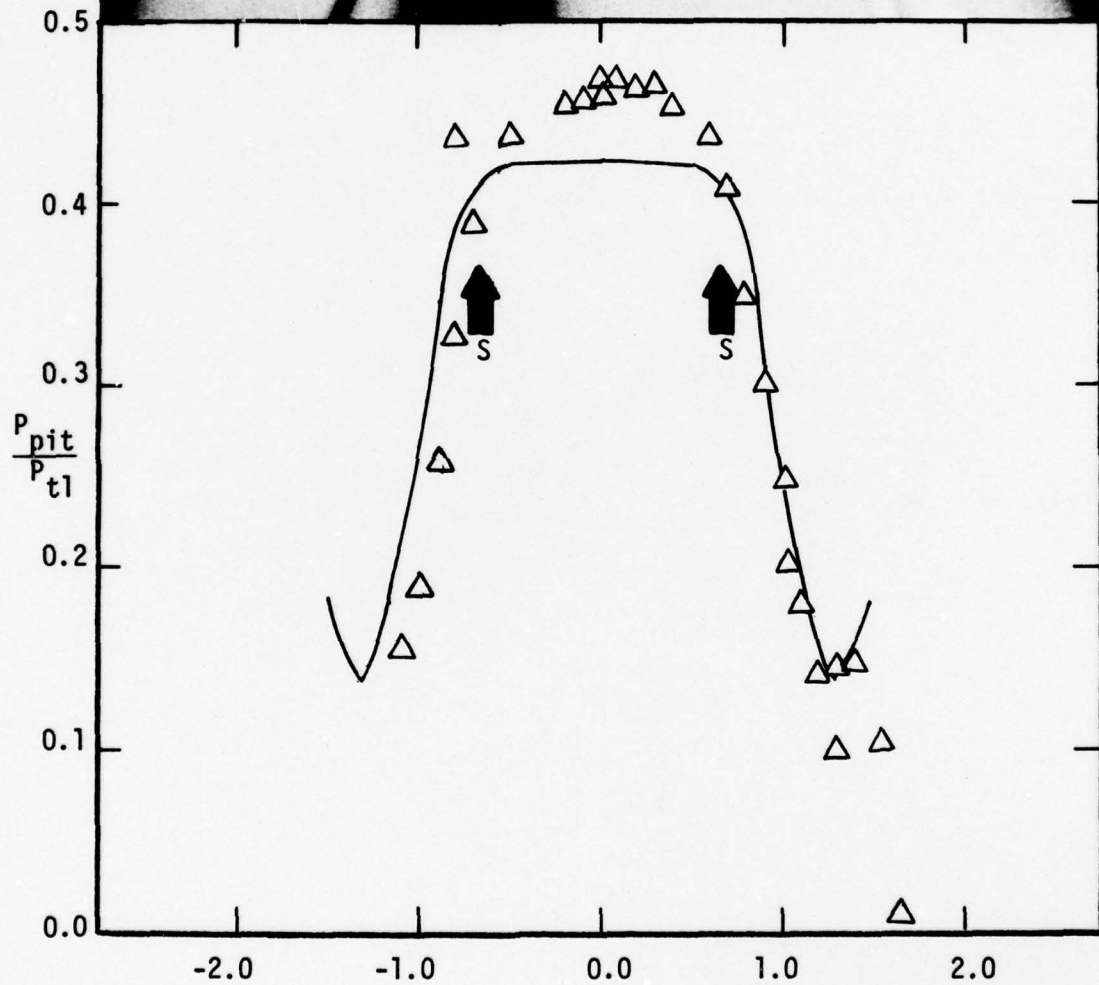
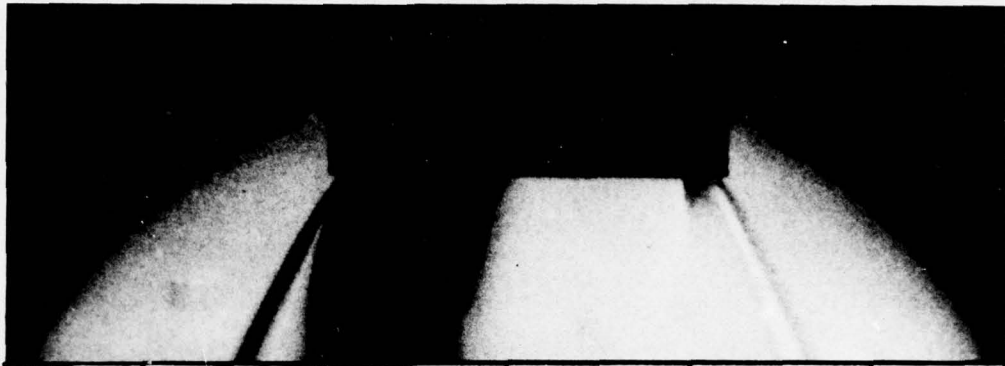
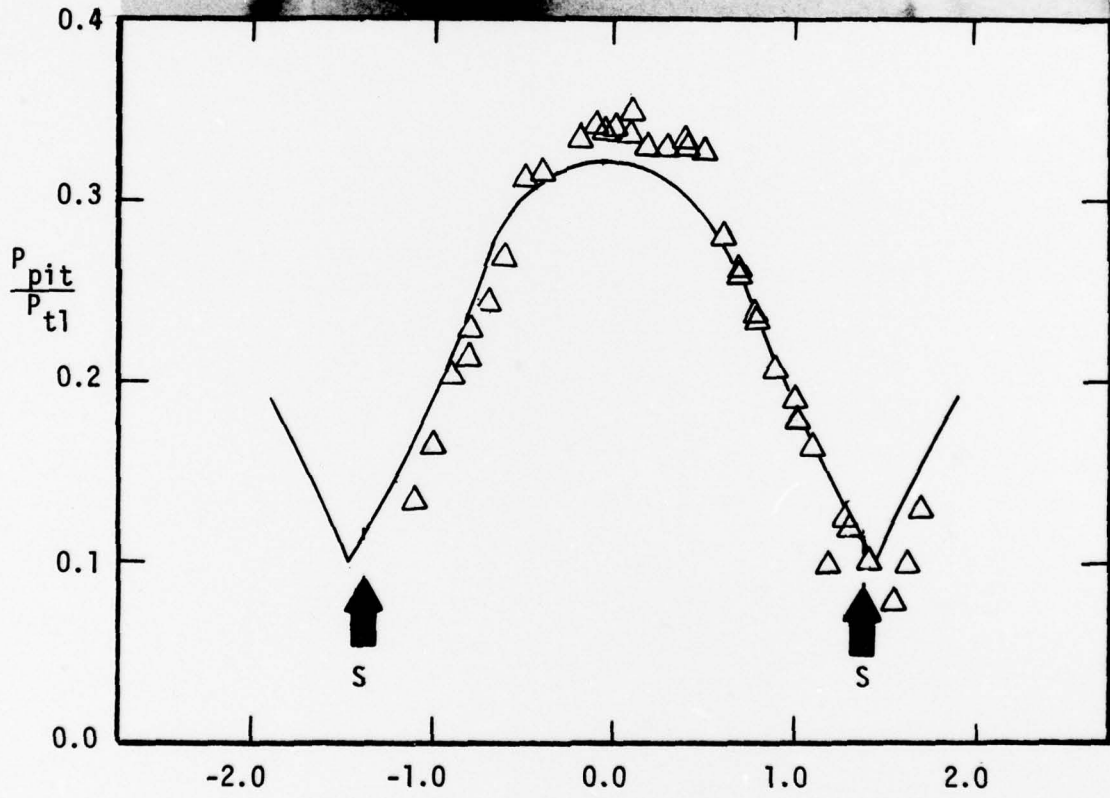
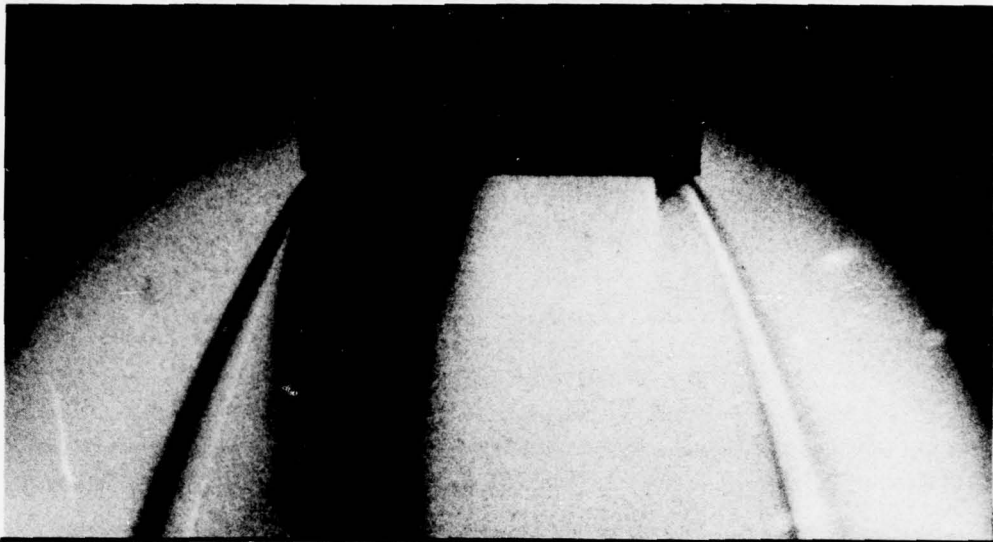


Figure 15. - The radial pitot-pressure distribution at downstream stations, 10° conical nozzle, $P_{t1} = 8.715 \times 10^6 \text{ N/m}^2$ (psia)



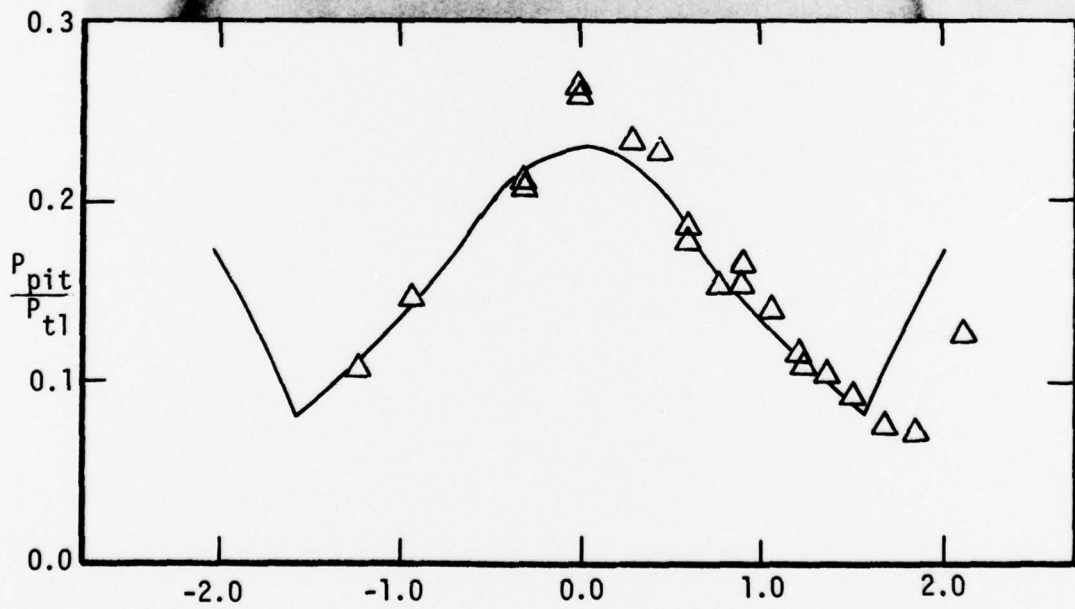
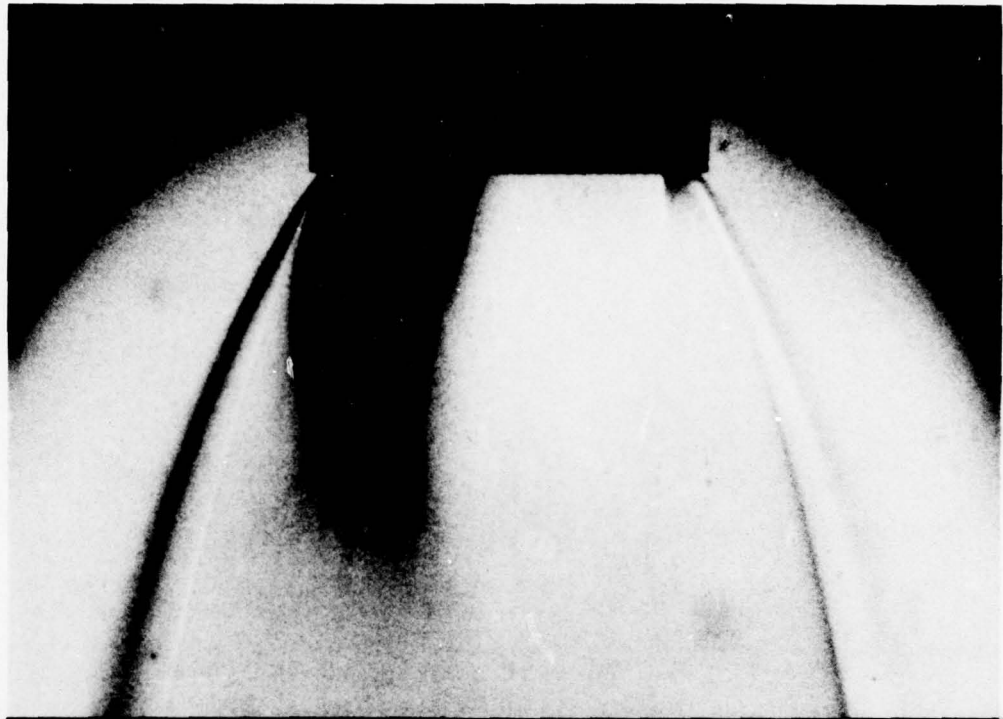
$$(b) \frac{\tilde{x}}{r_{ne}} = 1.0$$

Figure 15. - Continued



$$(c) \frac{\bar{x}}{r_{ne}} = 2.0$$

Figure 15. - Continued



$$(d) \frac{\tilde{x}}{r_{ne}} = 3.0$$

Figure 15. - Concluded

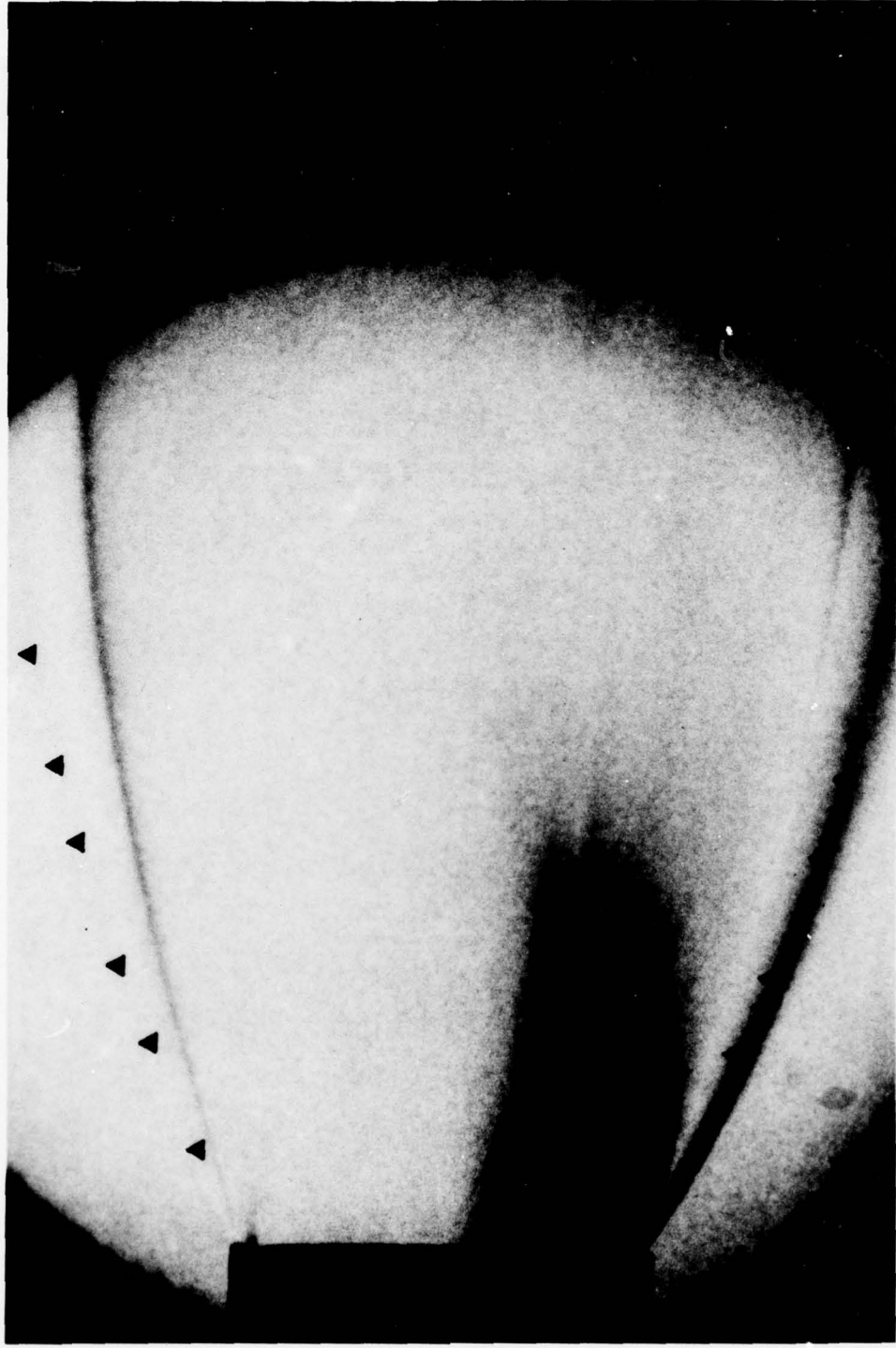


Figure 16. - Comparison of theoretical MOC solution with the experimental plume boundary of the 10° conical nozzle, $P_{t1} = 8.715 \times 10^6 \text{ N/m}^2$ (1264 psia)

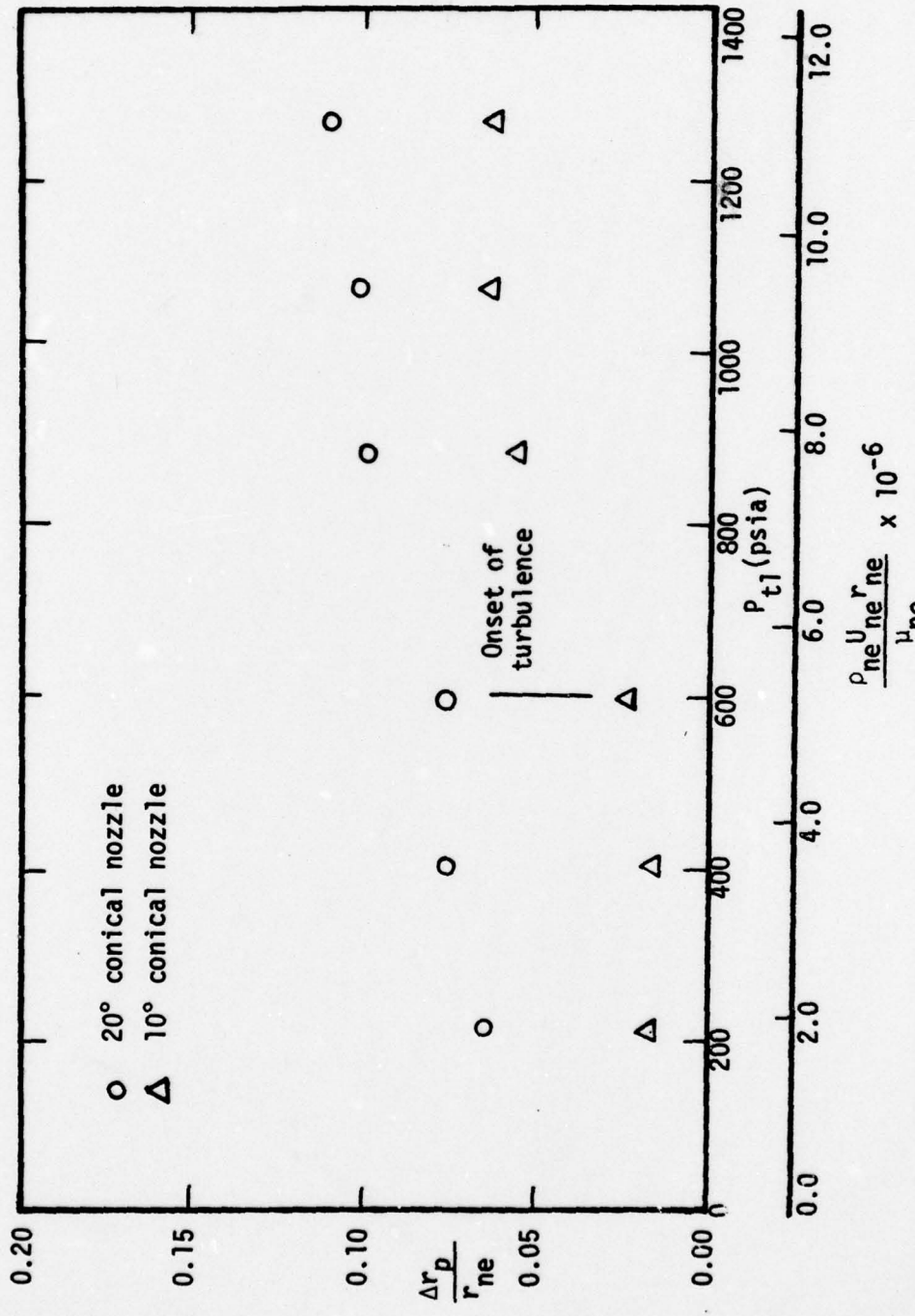


Figure 17. - Effect of the nozzle exit Reynolds Number on the location of the experimental plume boundary relative to the calculated inviscid boundary at $\tilde{x} = 1.0 r_{ne}$ for 10° conical nozzle and 20° conical nozzle.

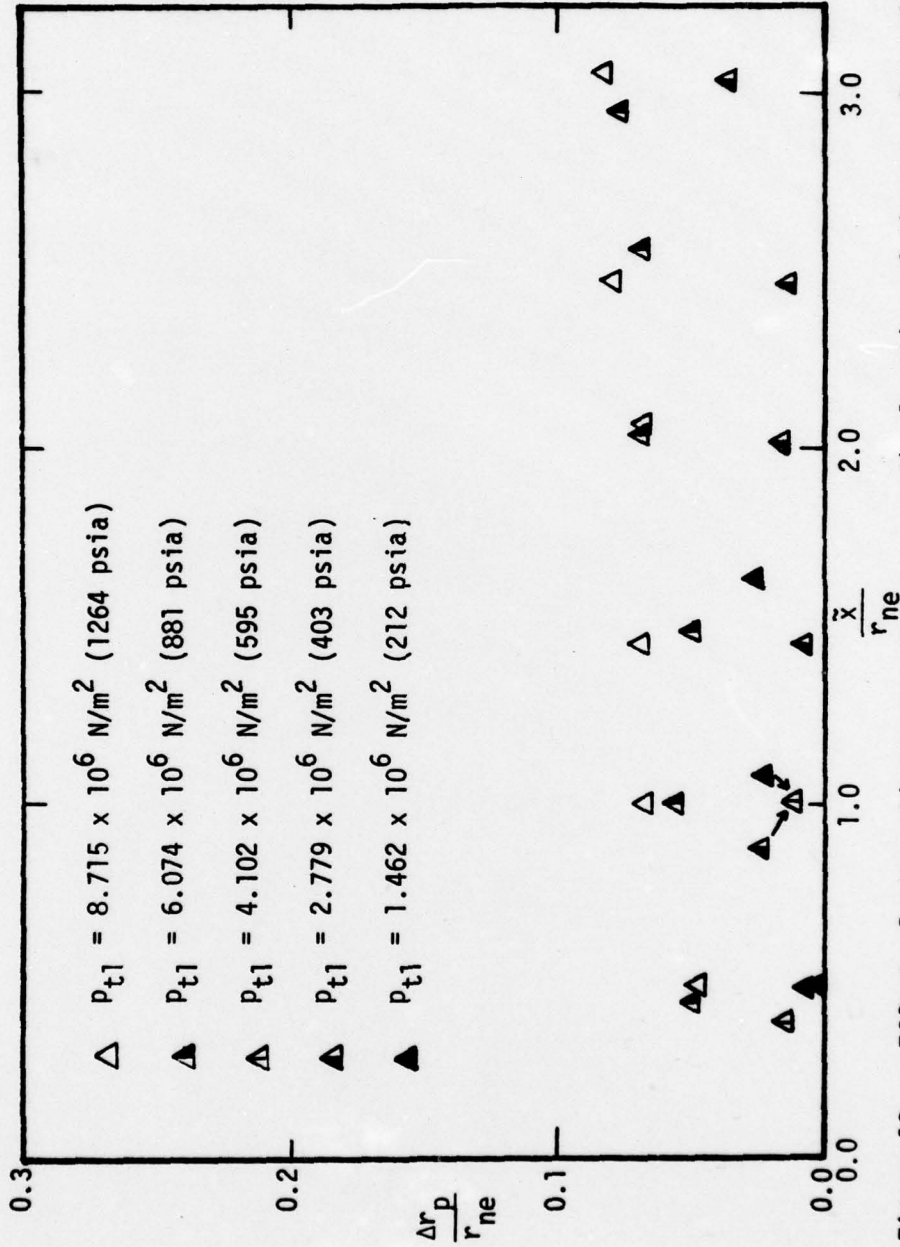


Figure 18. - Effect of stagnation pressure, P_{t1} , on the location of the experimental plume boundary relative to the calculated inviscid boundary at downstream stations for the 10° conical nozzle

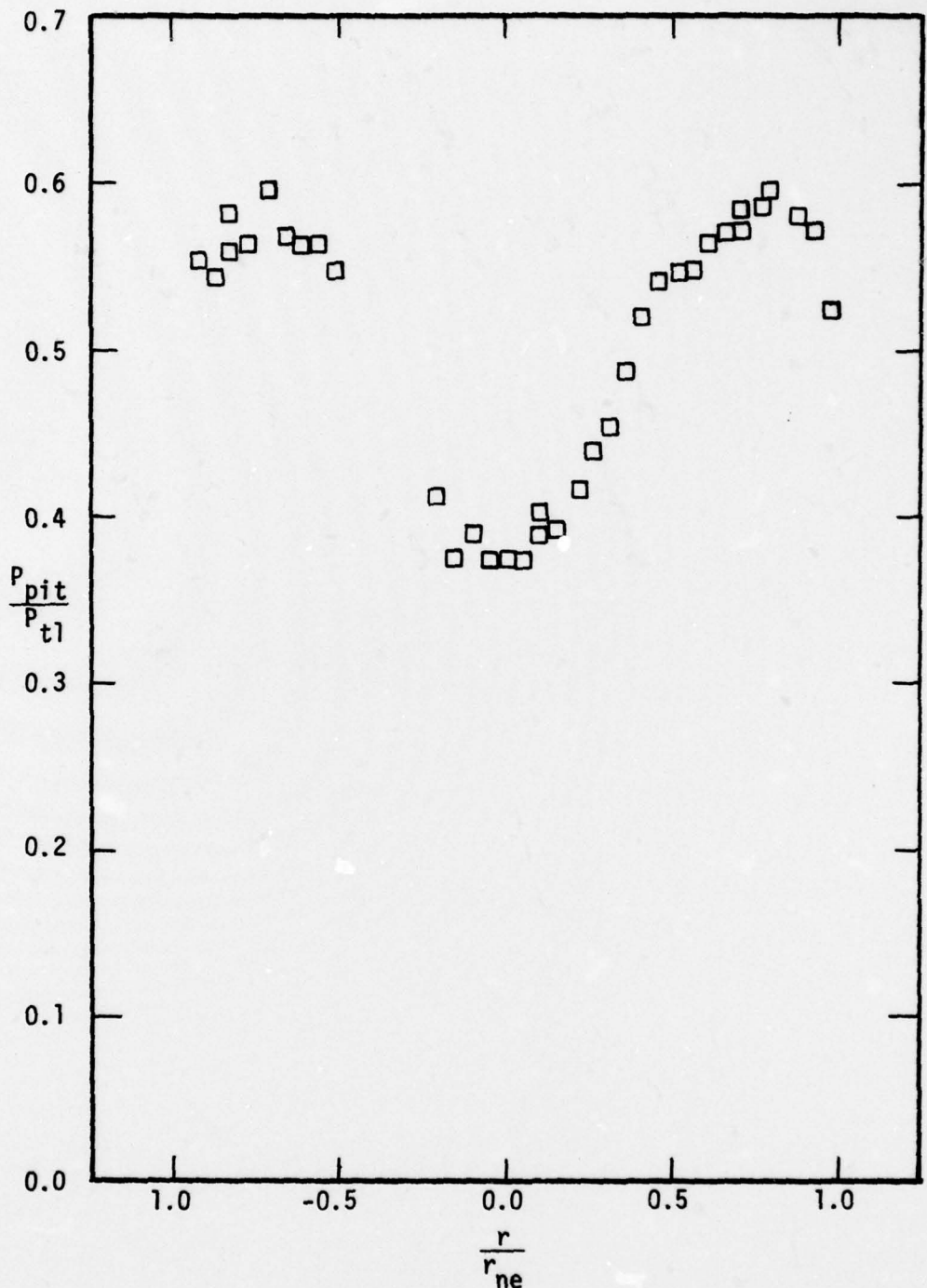


Figure 19. - Pitot-pressure distribution for the nozzle exit plane of 10° contoured nozzle, $P_{t1} = 8.715 \times 10^6 \text{ N/m}^2$ (1264 psia)

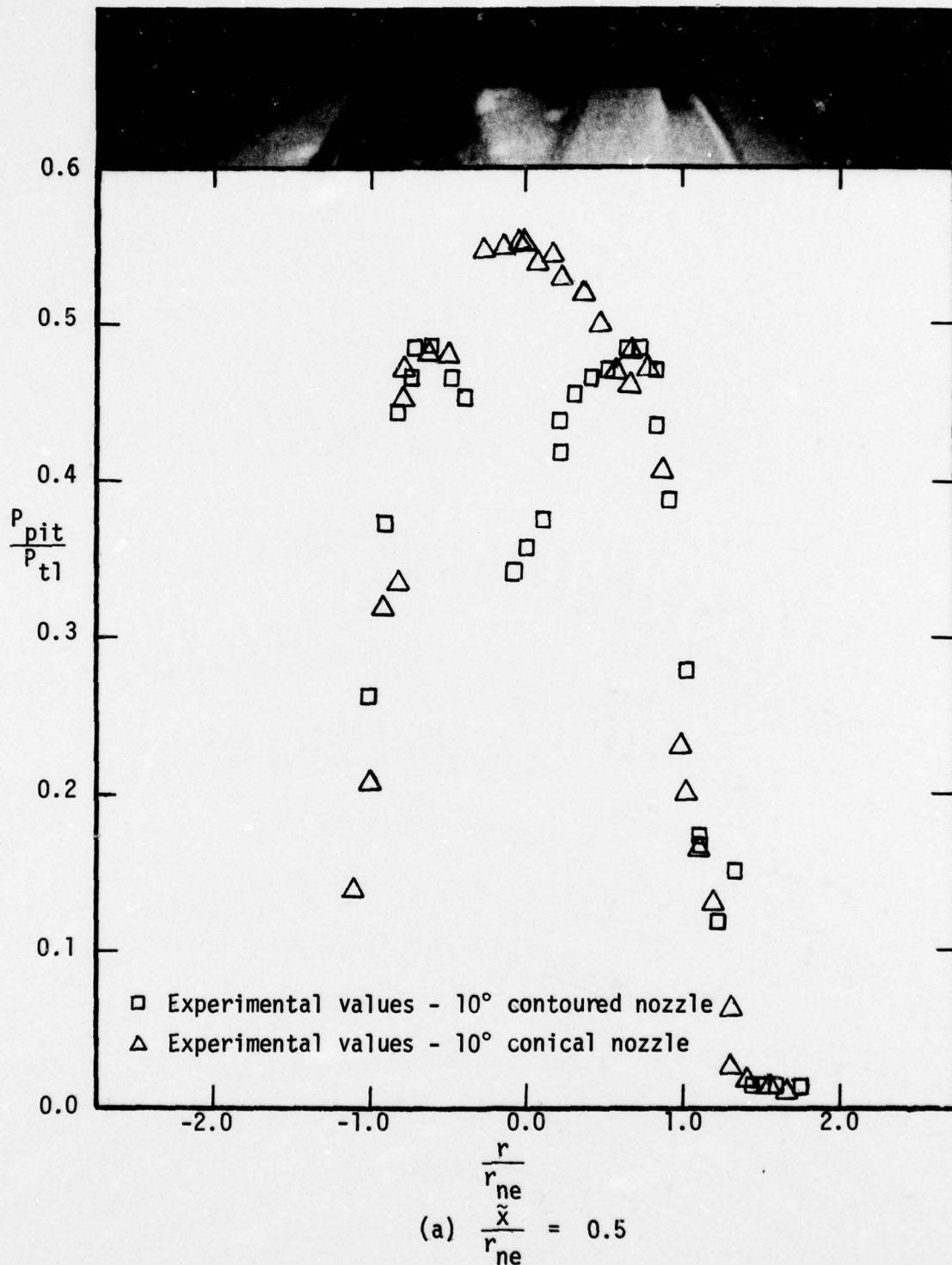
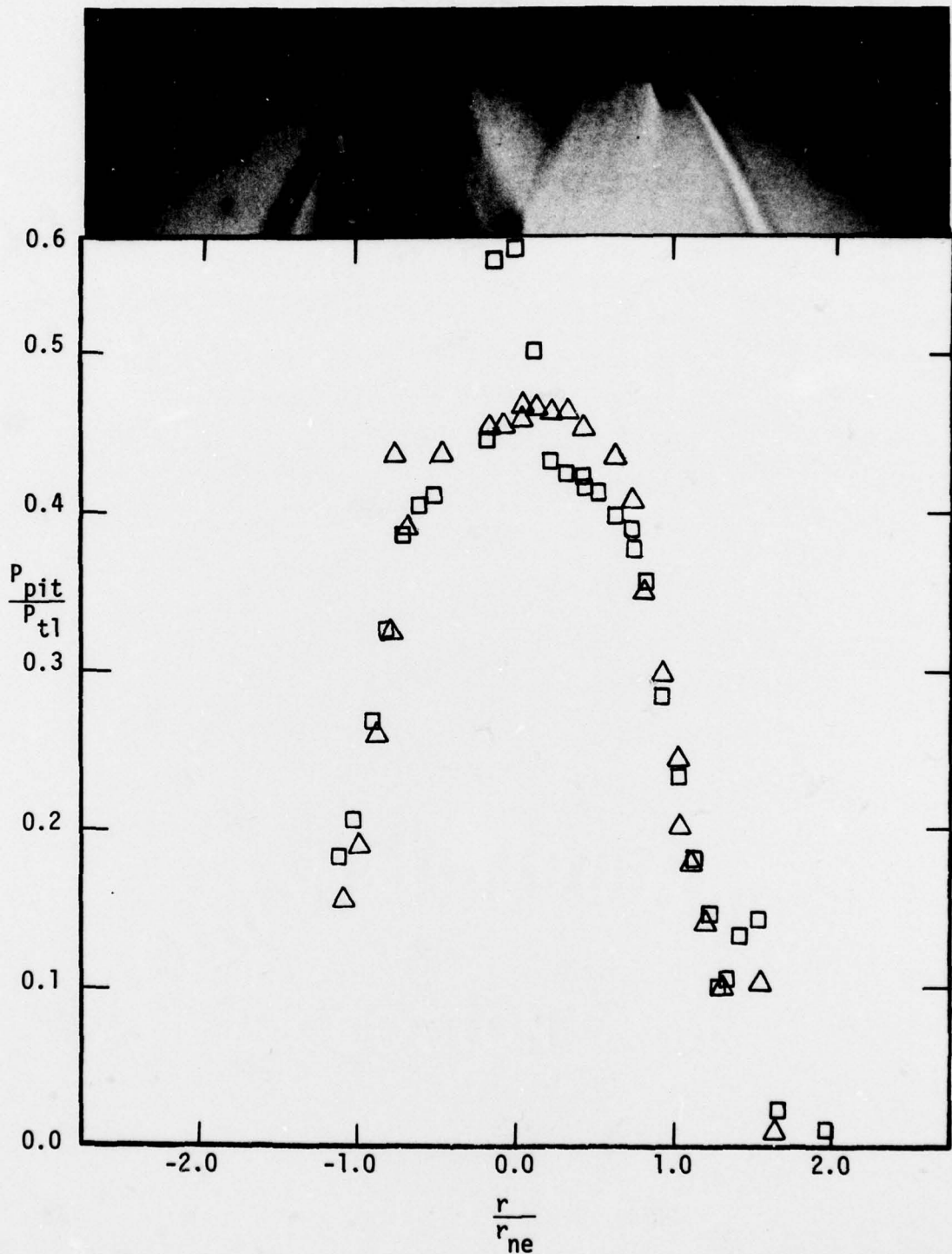
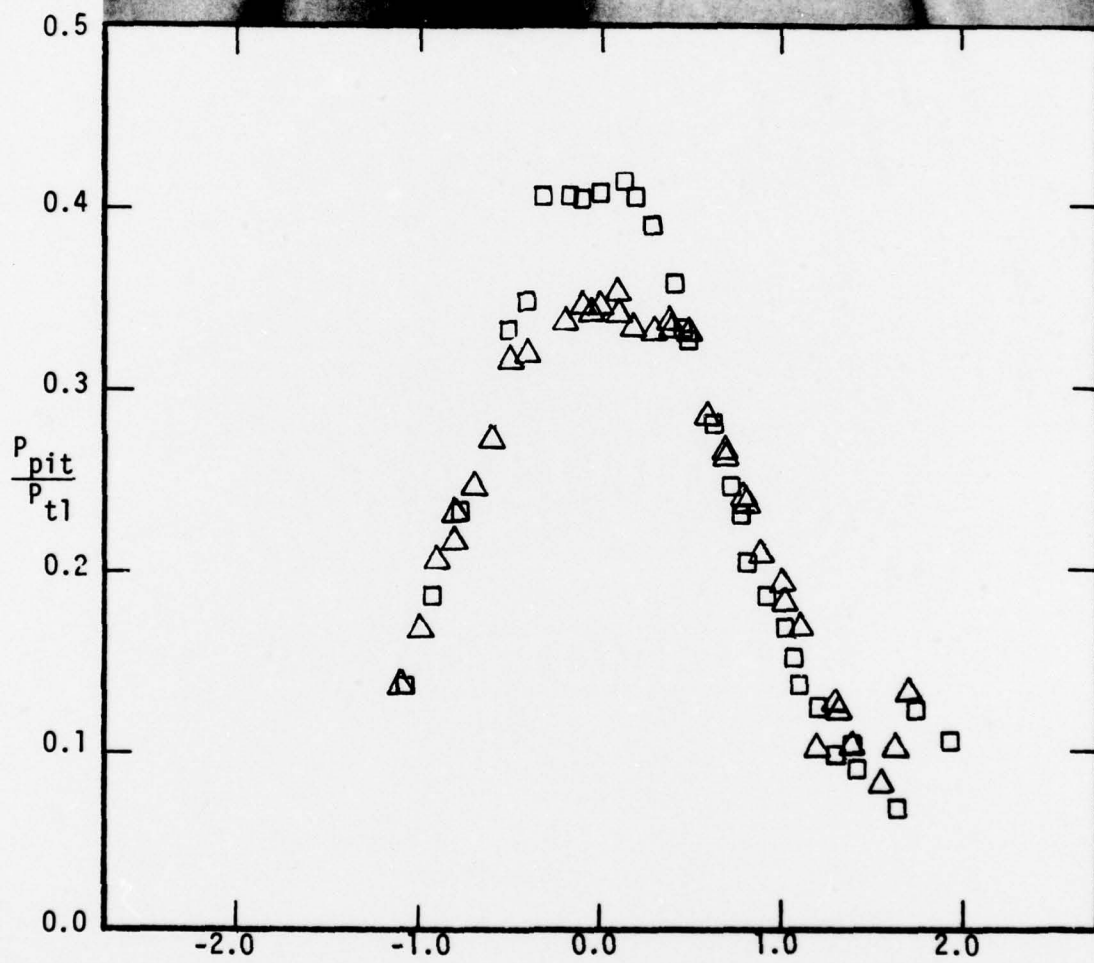
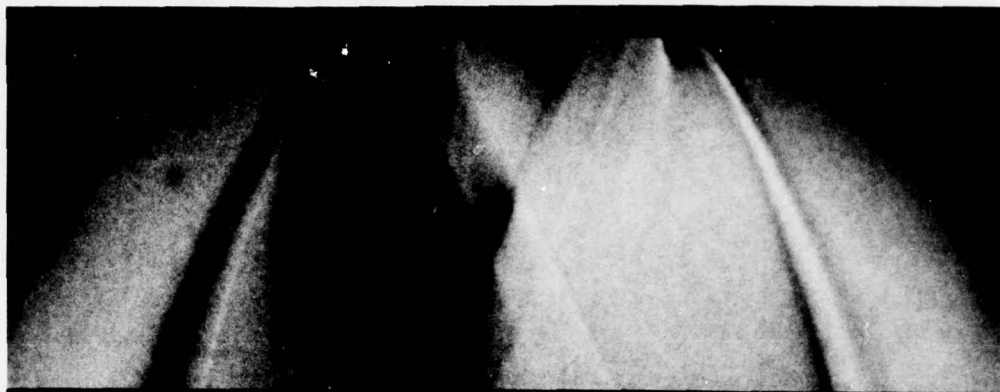


Figure 20. - The radial pitot-pressure distribution at downstream stations; 10° contoured and conical nozzles, $P_{t1} = 8.715 \times 10^6 \text{ N/m}^2$ (1264 psia)



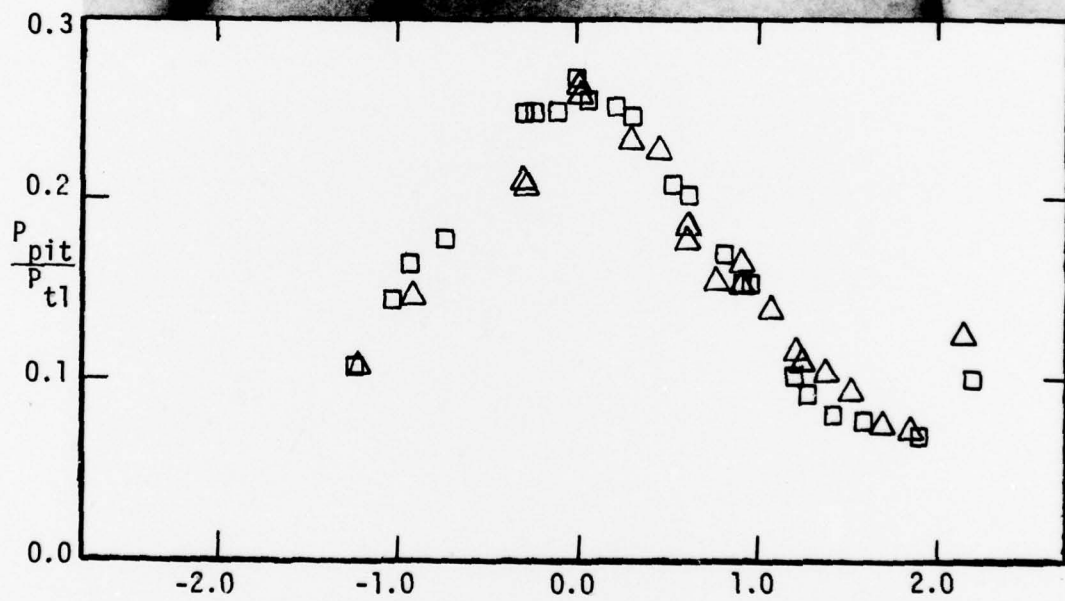
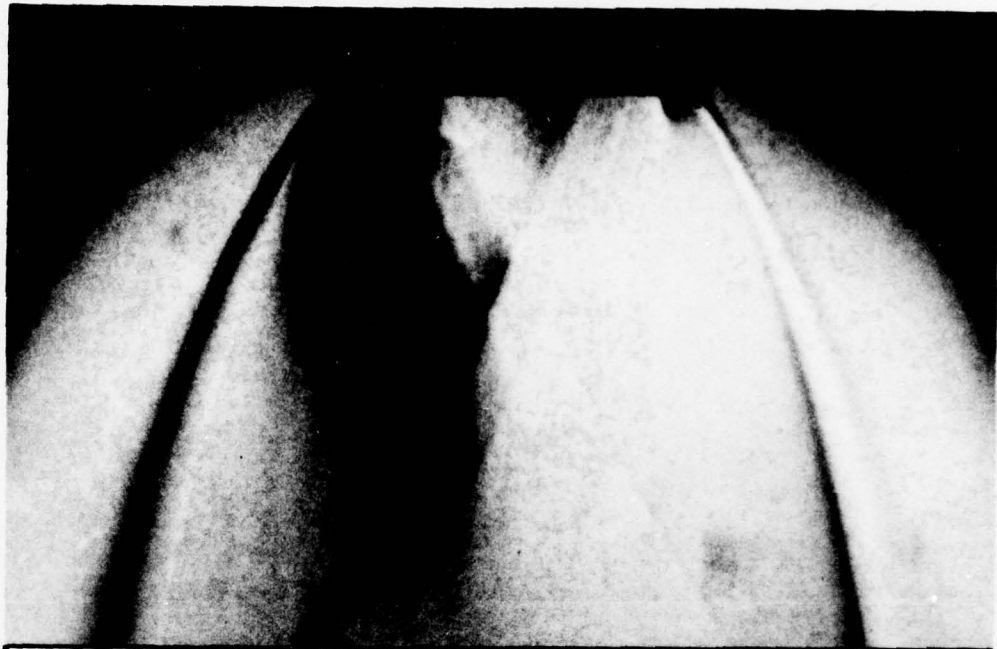
(b) $\frac{\tilde{x}}{r_{ne}} = 1.0$

Figure 20. - Continued



(c) $\frac{\tilde{x}}{r_{ne}} = 2.0$

Figure 20. - Continued



$$(d) \frac{\tilde{x}}{r_{ne}} = 3.0$$

Figure 20. - Concluded



Figure 21. - The experimental plume boundary for the 10° contoured nozzle, $P_{t1} = 8.715 \times 10^6 \text{ N/m}^2 \text{ (psia)}$

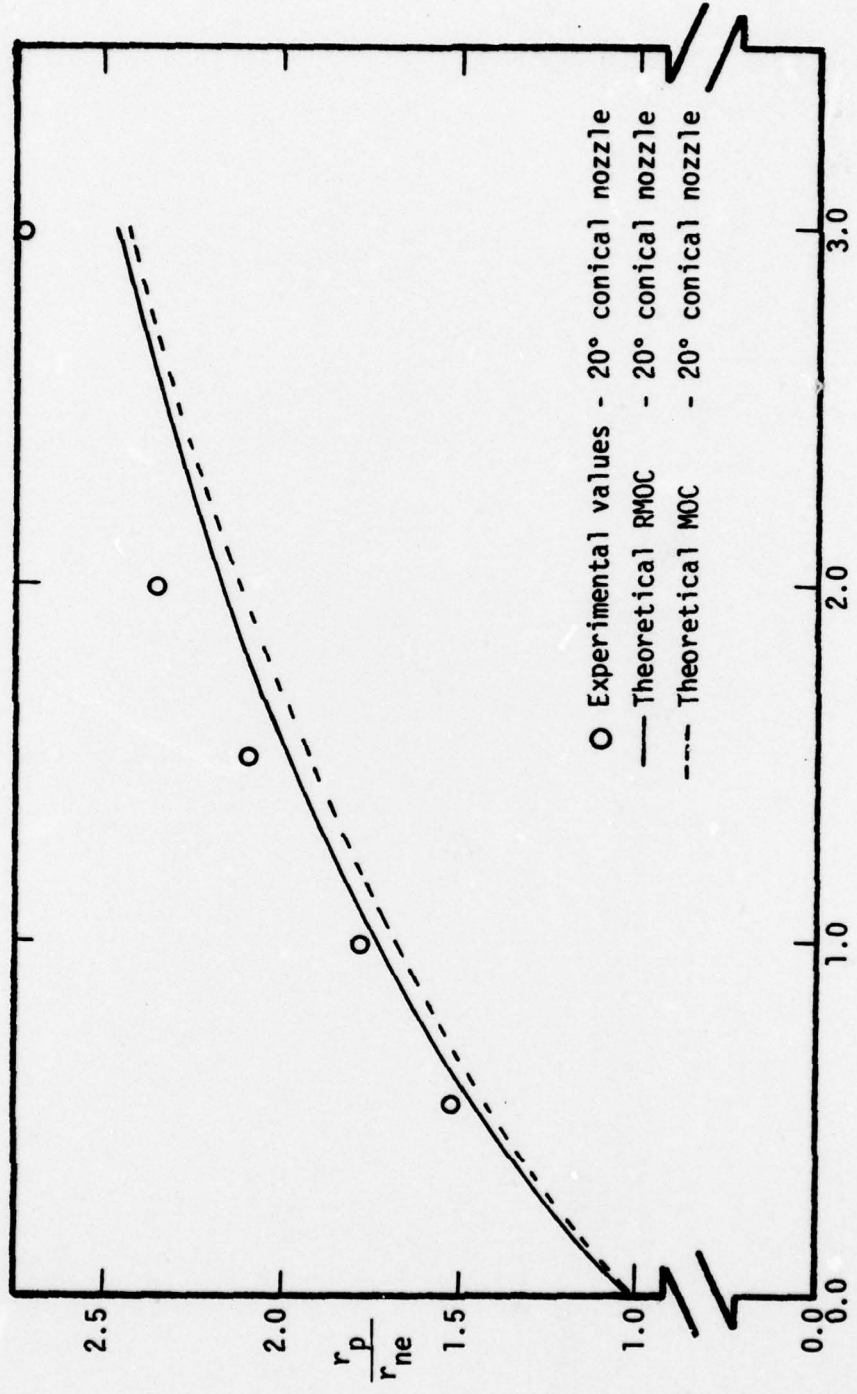


Figure 22. - Comparison of theoretical and experimental plume boundaries for the 20° conical nozzle, $P_{t1} = 8.715 \times 10^6 \text{ N/m}^2$ (1264 psia)

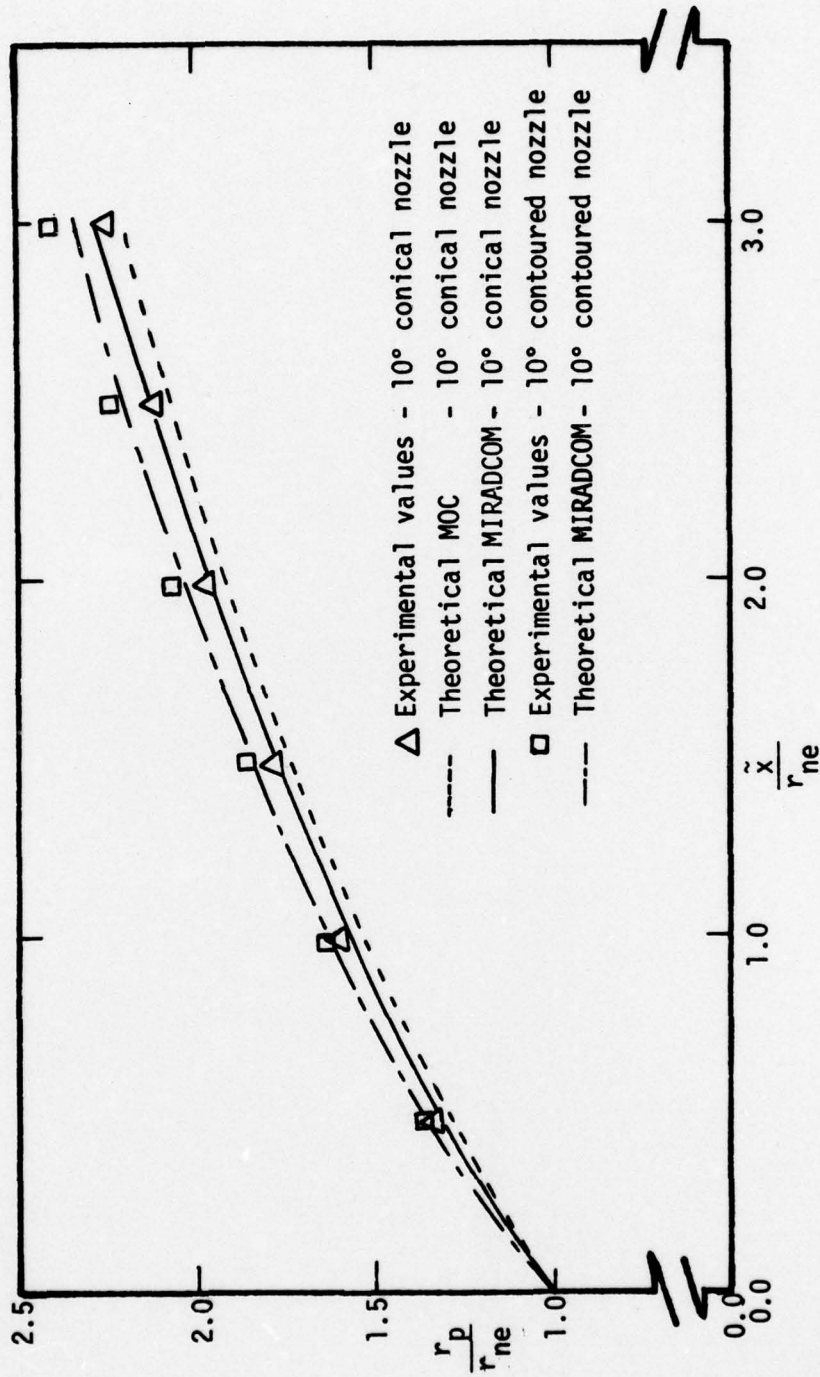


Figure 23. - Comparison of theoretical and experimental plume boundaries for the two nozzle configurations for which $\theta_{ne} = 10^\circ$, $P_{t1} = 8.715 \times 10^6 \text{ N/m}^2$ (1264 psia)

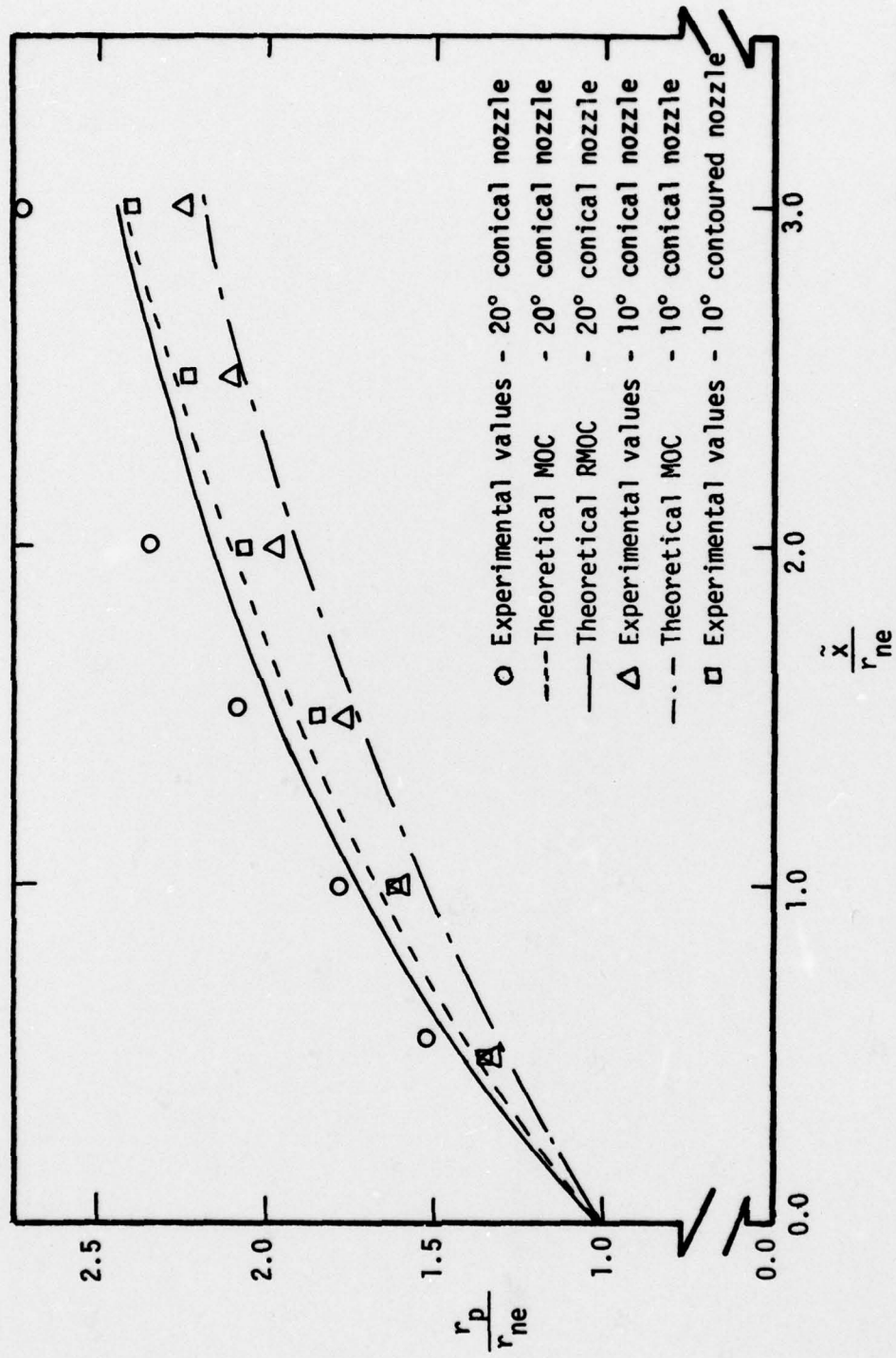


Figure 24. - Comparison of theoretical and experimental plume boundaries for the three nozzle configurations, $p_{t1} = 8.715 \times 10^6 \text{ N/m}^2$ (1264 psia)